

Optimization and Automation of the Spectroscopy Pipeline of the Falcon Telescope Network

Ted A. Reed¹, Markus D. Parrish¹, Joshua A. Key¹, Charles J. Wetterer², Philip J. Castro³,
David M. Strong⁴, Casey P. Schuetz-Christy¹, and Francis K. Chun¹

¹*Department of Physics and Meteorology,
US Air Force Academy, CO*

²*KBR, Kihei, HI*

³*Applied Optimization Inc., Fairborn, OH*

⁴*Strong EO Imaging Inc., Colorado Springs, CO*

ABSTRACT

The importance of space domain awareness has increased significantly with the growing reliance of satellites in our technological infrastructure. The United States Air Force Academy (USAFA) has been collecting spectral signatures to characterize satellites since 2014 using a 16-inch f/8.2 telescope (USAFA-16) on campus as well as its off-campus telescopes that comprise the Falcon Telescope Network (FTN). The FTN consists of 11 identical 20-inch, f/8 Officina Stellare ProRC-500 telescopes located at Sterling, CO; La Junta, CO; Durango, CO; Yoder, CO; Woodland Park, CO; Grand Junction, CO; State College, PA; Canberra, Australia; Gingin, Australia; Vicuna, Chile; and Braunschweig, Germany. The filter wheel contains B, V, R band Johnson-Cousins filters and a 100 lines-per-millimeter diffraction grating for low-resolution slitless spectroscopy.

Before using the FTN for satellite spectral observations, the diffraction grating used in each FTN telescope was spectrally calibrated by determining the pixel-to-wavelength conversion for each site. Known emission and absorption features from calibration stars are collected, and these features are used to build a relationship between pixels and wavelength; thereby, observations of satellite spectra can be displayed as a function of wavelength. Approximately half of the telescopes in the FTN have had their spectrum calibrated and are compared in this paper.

We automated, optimized, and standardized the manual steps within the processing pipeline to ensure the repeatability and improve the accuracy of the resulting spectra. First, we are investigating a new method for generating spectroscopic flat-fields to further improve its accuracy and the resulting accuracy of the satellite spectra. A method for spectroscopic flat-field correction was already established, but this paper describes a new and novel method for obtaining and applying a flat-field. Data were collected on an A-type star so that its zero and first-order spectra were allowed to drift across the entire length of the image. This process was repeated for different vertical positions to ensure that all pixels received a spectral band, and all positions were then repeated multiple times to average out atmospheric scintillation. All of the images were then compiled and averaged to build the spectroscopic flat-field. Second, we implemented a method to determine spectral features on a sub-pixel level using the Kwee-van Woerden method, increasing the precision of our pixel-to-wavelength calibration. Third, the atmospheric extinction theory has been developed and implemented. Calculating the atmospheric extinction involves observing a standard star throughout the night as its airmass varies. Fourth, we implemented solar analog normalization as a final calibration step. This involves observing solar analogs (e.g., G2V type stars) and normalizing the satellite spectra by the average solar analog spectra. This process removes the solar component of the reflectance spectra, leaving only the satellite component. These calibration enhancements are integrated into a new spectroscopic pipeline to process spectral signatures of geosynchronous satellites.

Additionally, a solar analog analysis was performed to assess the spectral type of stars used for solar analog normalization and attempt to constrain what spectral types are valid for this type of calibration. The spectra of solar-type stars (spectral types near G2V) were collected, extinction corrected, used to normalize a geosynchronous satellite, and the resulting solar analog normalized spectra were compared.

1. INTRODUCTION

Historically, the space environment was dominated by few nations: the United States, Russia, China, and the European community. The reliance upon satellite-provided information like weather forecasting, navigation, and telecommunications increased national and commercial interests in the space domain. The expanding number of satellites and space debris contributes to space congestion and elevates the need for Space Situational Awareness (SSA). Tracking and identification techniques are needed to provide SSA for both the United States Space Force and Air Force in this new war fighting domain. Low Earth orbit and Geosynchronous Earth Orbit (GEO) are of specific interest due to the number of satellites that are within these regions of space. A form of surveillance in this domain is through the use of optical telescopes. Spatially resolved imagery of satellites provides a great assessment of capability and function; however, telescopes with this ability are not always readily available. Using the small angle approximation, the angle needed to produce a resolved image of an object is described by Equation (1):

$$\theta \approx \frac{L}{d} \quad (1)$$

where L represents the size of the object, and d is the distance to the object. Satellites in GEO vary in size and are constrained by a limitation to resolved imagery as shown in Fig. 1 from [1]. Approximating the telescope's aperture as an Airy disk, the angular limit of resolution, is shown in Equation (2):

$$\varphi_{min} = 1.22 \frac{\lambda}{D} \quad (2)$$

where λ is the wavelength of light, and D is the diameter of the aperture. Distance and varying sizes of satellites in GEO limit telescopes when the angle needed to produce a resolved image is less than the angular limit of resolution. To combat this limitation, unresolved images of objects can be treated as a point source and require different techniques to characterize the satellite. The aim of the spectroscopy research conducted by the Center for Space Situational Awareness Research (CSSAR) is to obtain spectral signatures to characterize and classify satellites in conjunction with polarimetry and photometry efforts with the use of unresolved imagery. Diffraction gratings provide a spectrum to analyze the spectral characteristics of a satellite and may be used to classify and characterize.

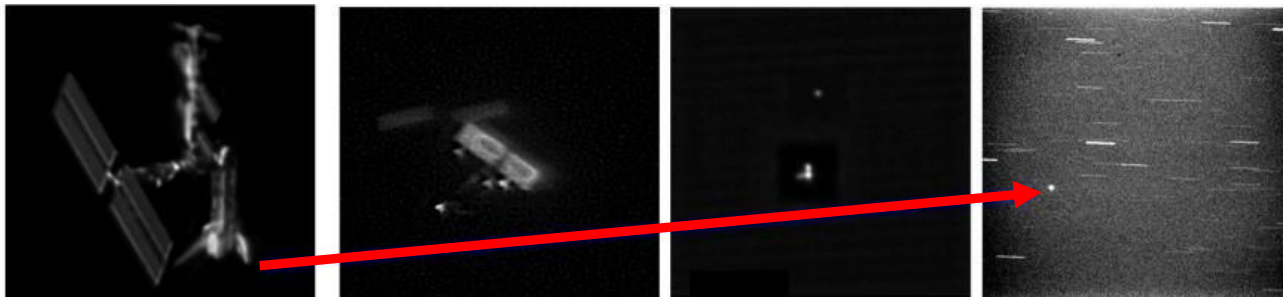


Fig. 1. Image showing the decreasing resolution of satellites as their distance increases.

Slitless spectroscopy, by way of diffraction gratings, can be used to collect the spectral signatures of satellites [2] [3] [4] [5] [6] [7]. This was shown to be a viable option to assess the spectral signature of a satellite during glint using the USAFA-16 and Falcon Telescope Network (FTN) telescopes [2] [3]. The FTN is a collection of 0.5-meter, $f/8$ Officina Stellare ProRC-500 telescopes that are spread across the world and used to collect optical signatures of satellites [8]. Table 1 shows the list of sites in the FTN. Previous CSSAR investigations into the use of a 100-lines-per-millimeter diffraction grating were to collect and calibrate slitless spectral observations, account for pixel response as a function of wavelength for two FTN sites, and process the spectrum of satellites in GEO [3].

Table 1. FTN Locations

	Name	Location
CBR	Canberra	Canberra, Australia
CMU	Colorado Mesa University	Grand Junction, CO
FLC	Fort Lewis College	Durango, CO
FRH	Farish Recreation Area	Woodland Park, CO
MMO	Universidad de La Serena	Vicuna, Chile
NJC	Northeastern Junior College	Sterling, CO
OJC	Otero Junior College	La Junta, CO
PSU	Pennsylvania State University	State College, PA
TUBS	Technische Universität Braunschweig	Braunschweig, Germany
UWA	University of Western Australia	Gingin, Australia
YDR	Yoder	Yoder, CO
USAFA-16	US Air Force Academy 16" telescope	US Air Force Academy, CO

Fig. 2 outlines the steps within the USAFA slitless spectroscopy pipeline. As with any Charge Coupled Device (CCD) image, the first step is bias and dark subtraction. Next, the image needs to be flat-fielded, but unlike a photometric image, the spectroscopic image has effects determined by the location of both the 0th order and 1st order spectrum on the image, thus requiring more complex processing. The novel approach developed here is described in Section 2. Next, the spectra itself is extracted from the image and a pixel-to-wavelength calibration is accomplished. The theory behind this is first described in Section 3.1, and an improved approach of achieving sub-pixel resolution for spectral features is described in Section 3.2. The new results of using spectral calibration stars (e.g., A-type main-sequence stars and Wolf-Rayet stars) observed by the FTN to determine the instrument specific “slope” and “offset” are detailed in Section 3.3. The resulting instrumental flux (in counts per second) as a function of wavelength can be corrected for atmospheric extinction using an extinction vs. wavelength relation and the observed airmasses of each image. The extinction versus wavelength relation is determined by observing standard stars over a range of airmasses. The theory behind this is first described in Section 4.1, and the results of this extinction calculation for two stars observed from an FTN site is described in Section 4.3. The process of creating a solar analog spectrum by observing solar analog stars and taking an average spectrum is demonstrated in Section 5. As an example of the calibrations performed on a GEO satellite in the spectroscopy pipeline, the instrumental, extinction corrected, and solar analog normalized spectrum for a GEO satellite (DTV-10) is presented in Section 6. A solar analog analysis is performed by observing 24 solar-type stars (spectral type F2V to K0.5V), their spectra is extinction corrected, used to normalize a GEO satellite, and the resulting solar analog normalized spectra are compared in Section 7. Finally, the summary and future work are provided in Section 8.

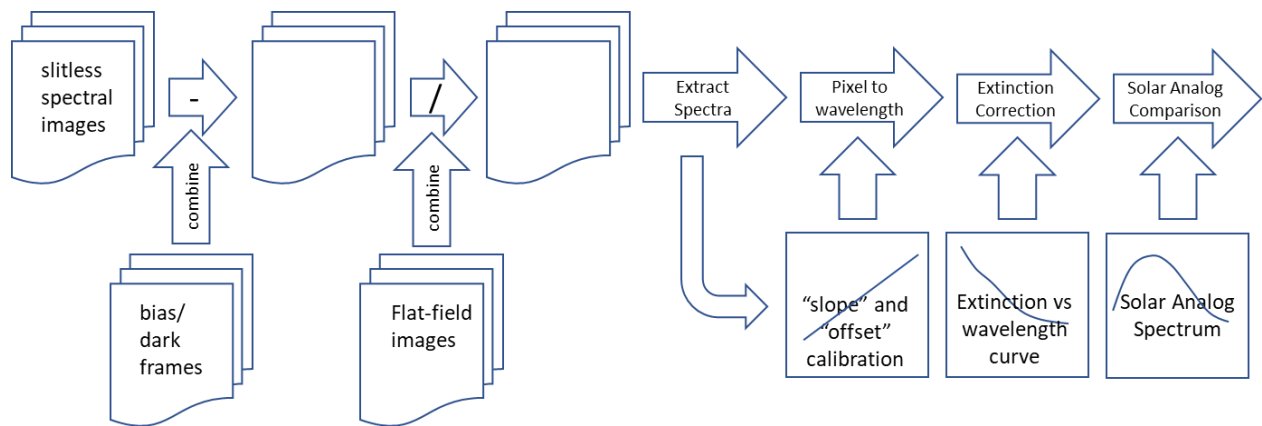


Fig. 2. USAFA slitless spectroscopy pipeline.

2. FLAT-FIELD CORRECTION

Small variations in pixel sensitivity, optical path aberrations, and geometric properties of the camera cause different regions of the image to record unequal amounts of light in what would be an otherwise evenly illuminated image. While flat-field correction is a common practice for photometric imaging, the application to spectroscopic imaging is more complicated and will be improved upon using a new technique. Previously, a technique using broadband flat-field images to map out the pixel-by-pixel response as a function of wavelength was employed [2], but this neglected to separate the contribution related to the geometry of the telescope before the diffraction grating and vignetting (thus, related to the spectrum's 0th order) and the contribution after the diffraction grating and the CCD itself (thus, related to the spectrum's 1st order).

We implemented a novel flat-field correction approach to further increase the accuracy of our data. Images taken with the USAFA-16 telescope are used to demonstrate the process. To build the flat-field, a series of 90-second exposure images were taken with the telescope drive off to allow a 3rd magnitude star near the zenith to drift across the entire image as seen in Fig. 3. The vertical banding in the 1st order streak is caused by scintillation of the star by the atmosphere, so five images were taken at the same declination and combined to reduce this effect. The amplitude variation of the remaining scintillation was determined and removed. In order to cover all portions of the CCD, scans for five declinations were collected. The horizontal banding seen in the image corresponds to absorption bands in the star's spectrum.

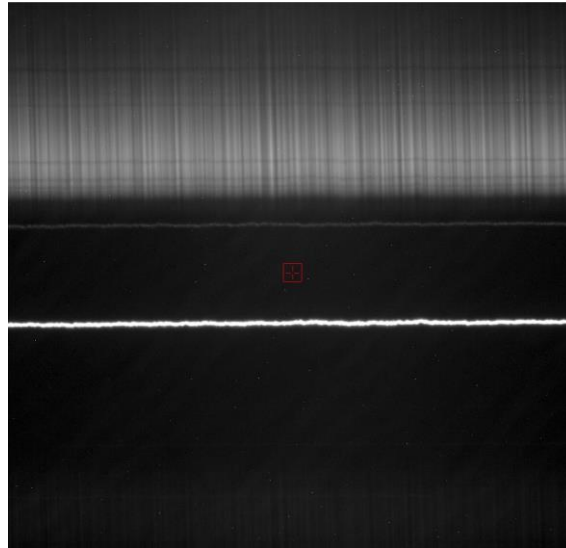


Fig. 3. Image with tracking off, allowing the zeroth order and its spectra to streak across the entire field.

Two separate flat-fields were created from the resulting scans. One corresponding to the location of the 0th order on the image, and the second corresponding to the location of the 1st order on the image. The 0th order correction (related to the large-scale structure flat-field) accounts for changes in brightness to the overall spectra determined by the light path up to the diffraction grating (e.g., vignetting caused by the telescope optics), while the 1st order correction (related to the small-scale structure flat-field) accounts for changes in brightness due to pixel-to-pixel variations on the image plane (e.g., pixel sensitivity).

First, for each scan, the relevant flat-field sub-image was generated by creating a map to calculate the wavelength of each pixel and then dividing by the average spectra of the star on a pixel-by-pixel basis. This map depends on the pixel-to-wavelength conversion slope and offset for the particular site, the alignment of the celestial sphere with respect to the CCD (determined from the angle the 0th order tracks across the CCD), and the alignment of the diffraction grating with respect to the CCD (determined from the angle of the scintillation pattern in the 1st order spectra). Next, the large-scale structure flat-field was generated from each scan by smoothing the image with a moving mean of 200 pixels. Finally, the corresponding small-scale structure flat-field was generated by dividing the

flat-field sub-image by the large-scale flat-field for that scan. Two of the five flat-field sub-images, large-scale flat-fields and small-scale flat-fields generated from the USAFA-16 scans are shown in Fig. 4.

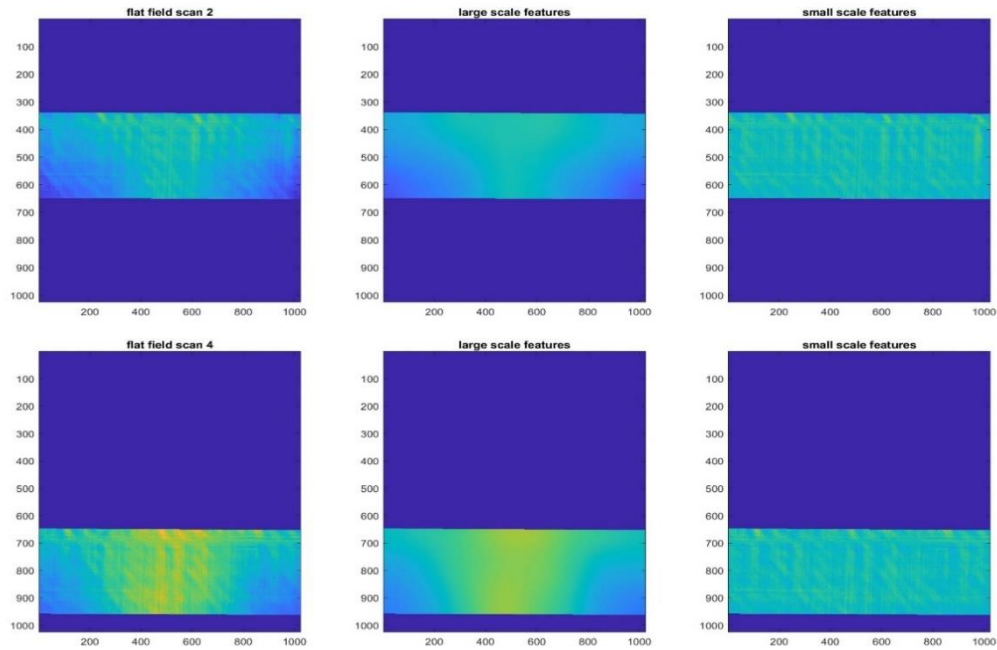


Fig. 4. Flat-field sub-image (left), large-scale flat-field (center), and small-scale flat-field (right), for scan 2 (top) and scan 4 (bottom).

The small-scale flat-field scans can be directly combined pixel-by-pixel, as shown in Fig. 5, and the resulting small-scale flat-field can be used directly on each subsequent image as a regular photometric flat-field image. Positions outside of the scans are assigned a value of one but also correspond to regions of the CCD that will not be used to image a 1st order spectrum. The vertical features in the small-scale flat-field are artifacts of the scintillation of the star during the scans that were not fully removed during the processing. The horizontal features in the small-scale flat-field are artifacts from the pixel-to-wavelength conversion and the absorption features present in the A-type star used to generate the flat-field. The diagonal features are the small-scale flat-field features we are attempting to map and take into account.

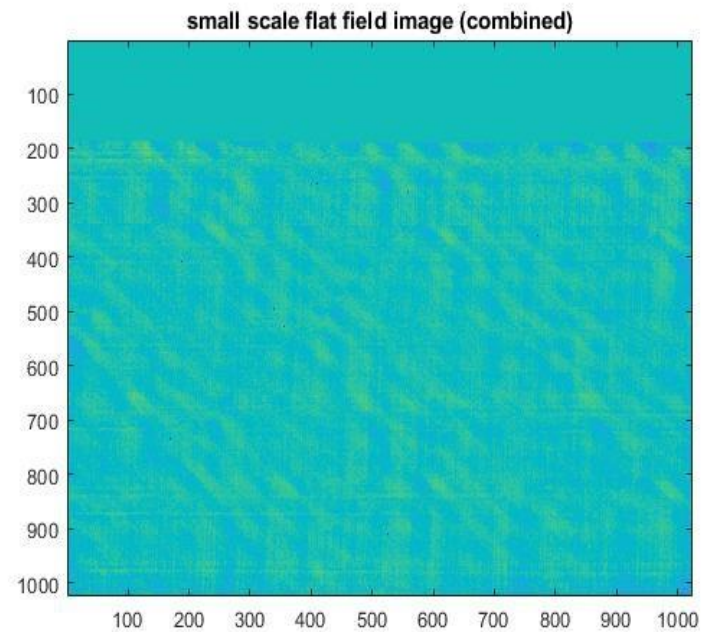


Fig. 5. The small-scale flat-field.

Each scan corresponds to the 0th order at a particular vertical pixel position. For a given image, the large-scale flat-field can be generated, and is the interpolation between the appropriate scans according to the vertical position of the 0th order and the values corresponding to the horizontal position of the 0th order. The resulting large-scale flat-field scaling is then applied to the star spectra itself after extraction as a function of wavelength.

A series of 1-second exposure images were taken to be used as a means of testing the resulting flat-field. The 0th order and 1st order spectra were positioned in different parts of the CCD image, taking 18 sets of five images and combining the five images per set to reduce error. The spectra extracted from all the image sets are shown in Fig. 6 with the difference between individual spectra being up to six percent, as shown in the right-hand plot.

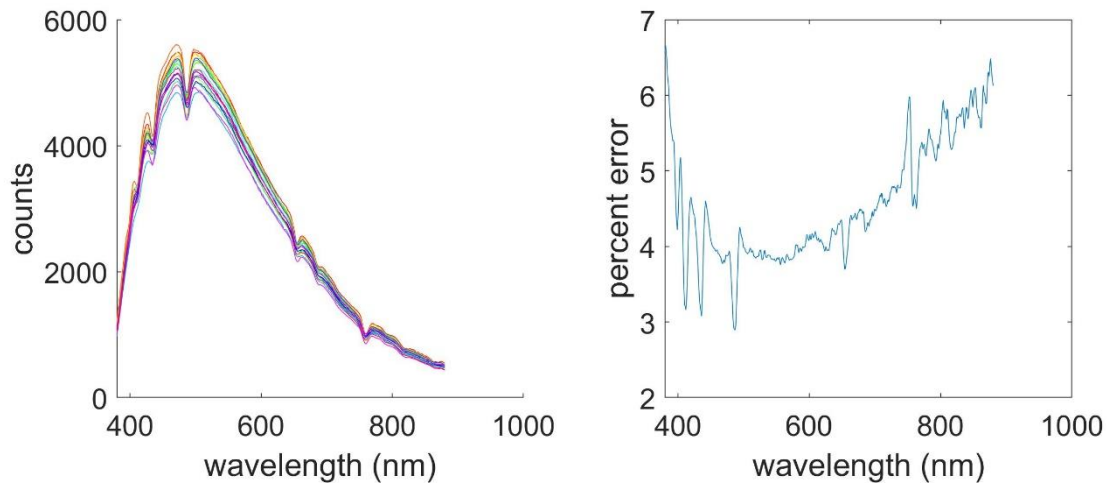


Fig. 6. Spectra of the same star taken in different regions of the CCD (left) and the percent error as a function of wavelength for these same spectra (right).

If no flat-field correction needs to be made, all spectra in Fig. 6 would theoretically align perfectly assuming a photometric night and no atmospheric extinction changes. Unfortunately, it was determined that the night in question was not photometric, so the up-to-six-percent differences observed were not due to the flat-field but rather due to the atmosphere. Whereas this does not allow us to test the large-scale flat-field, by normalizing all the spectra and comparing the results, the small-scale flat-field can be assessed. Fig. 7 compares the before (top) and after (bottom) normalized spectra where the spectra are shown on the left and the percent error as a function of wavelength are shown on the right. The small-scale flat-field correction was not as significant as desired. Whereas the average percent error before processing is 1.67%, the average percent error after flat-field correction is 1.60%. Additional observations and more work needs to be done to assess this technique of spectroscopic flat-field correction and fully add it into the USAFA spectroscopy pipeline.

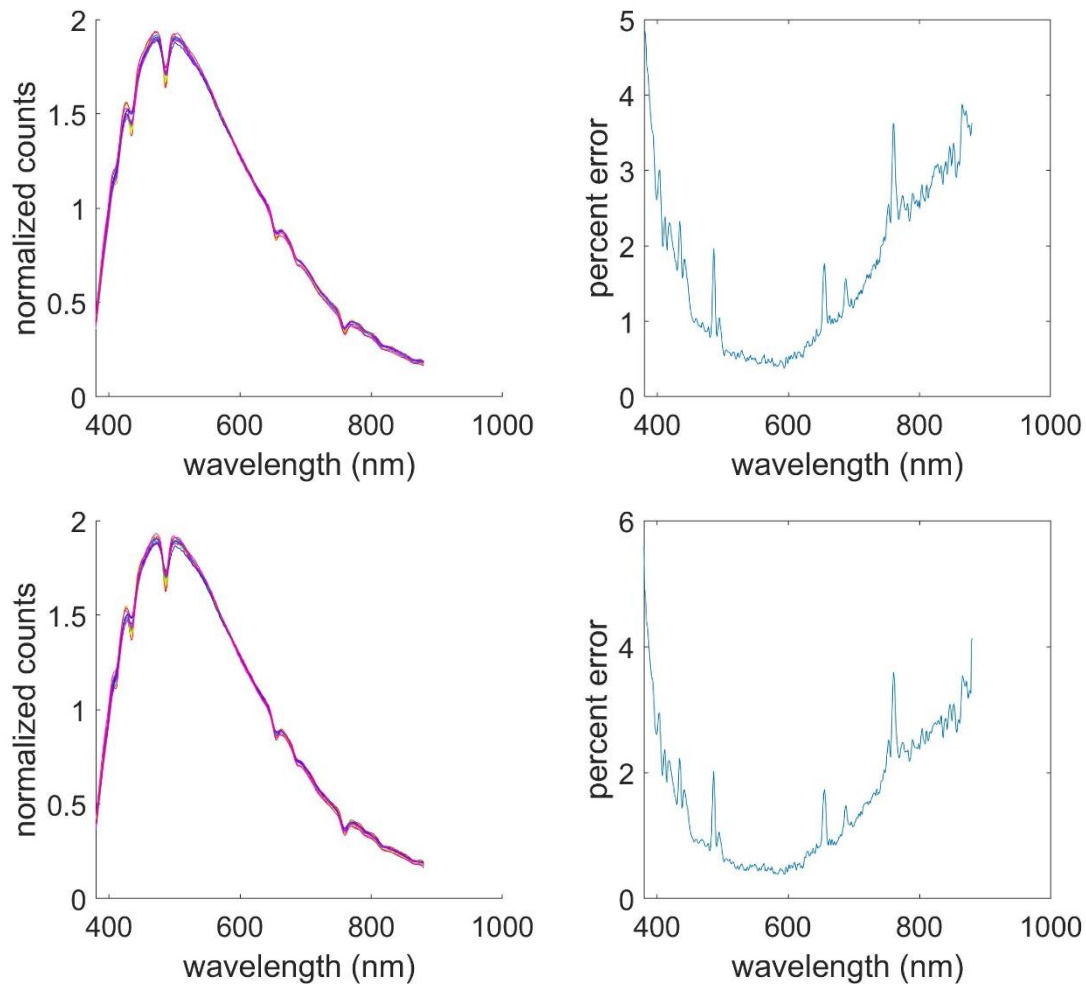


Fig. 7. Normalized spectra of the same star taken in different regions of the CCD (left) and the percent error as a function of wavelength for these same spectra (right), both before (top) and after (bottom) flat-field correction.

3. PIXEL-TO-WAVELENGTH CONVERSION

The FTN is fitted with a 100 lines/mm diffraction grating in one of the filter-wheel positions that creates an interference pattern on the image plane. Both the 0th order and 1st order spectrum of a star or object is imaged. For a satellite, the electro-magnetic radiation is reflected sunlight as shown in Fig. 8, and thus the spectrum will closely match that of the Sun with modifications associated with the reflecting material. When the angle of incidence equals the angle towards the observer with respect to the normal of a surface on the satellite, the brightness is greatly enhanced, and this is known as a glint. Reflections and glints off different satellite surface materials will lead to variations in the resulting spectrum.

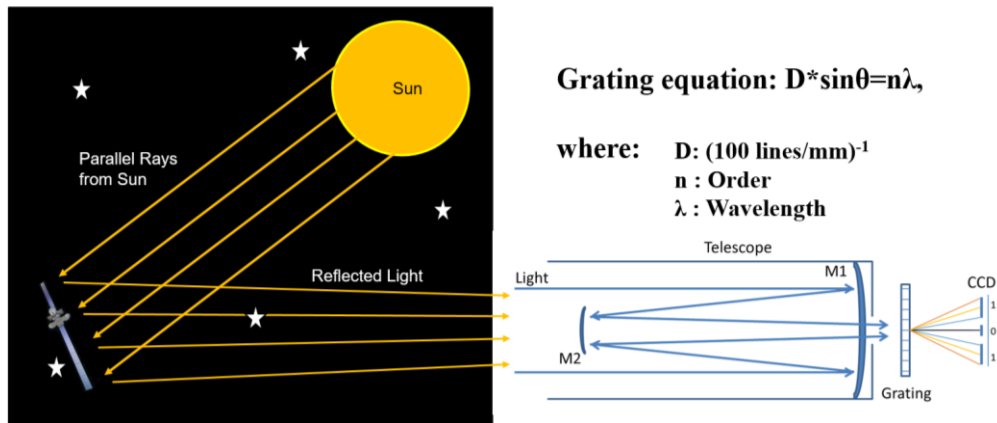


Fig. 8. Schematic setup of the FTN measuring the reflected light from the satellite using a diffraction grating.

A sample image of two GEO satellites is shown in Fig. 9. The satellite to the right is MEXSAT-3, and the satellite to the left is EUTELSAT 115 WEST B. The 0th order is the bright spot, here at the top of the image, and the 1st order is the spectrum of the object below the 0th order. The horizontal streaks are the 0th order of faint stars. The spectra are extracted from each spectral image by aligning and clipping the images as shown in the first steps of Fig. 10. The result is a spectrum in counts (or equivalently counts per second if divided by the exposure time) as a function of pixel position. Specifically, the spectrum is the average count of the central 10 pixels minus the median value on either side to account for the sky background pixel by pixel along the 1st order.

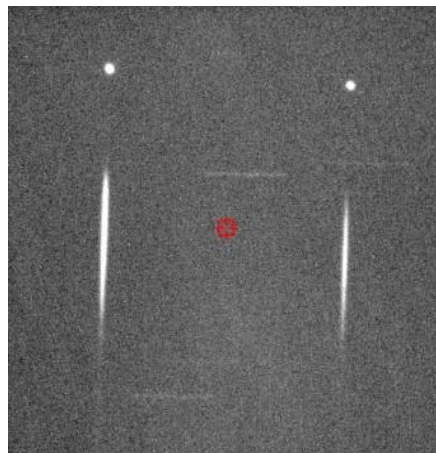


Fig. 9. Raw image collected from the USAFA-16 telescope that displays the spectral image of two satellites.

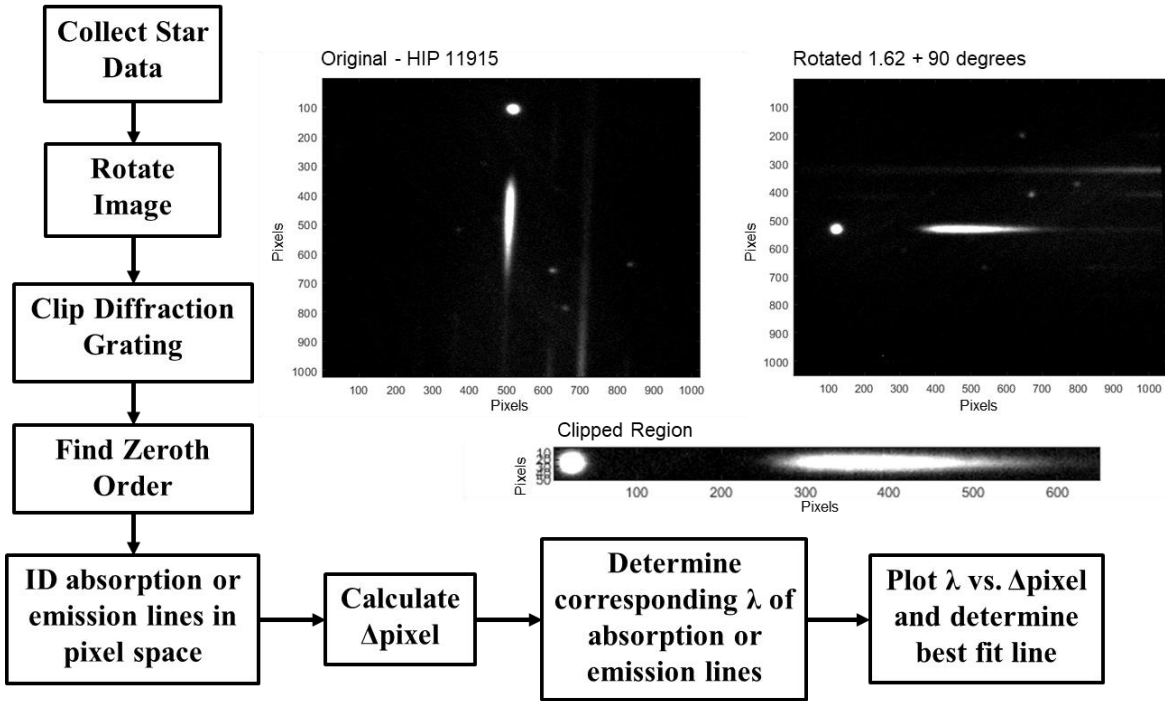


Fig. 10. Diagram of the pixel-to-wavelength conversion showing the process of cropping the images to align the pixels with the corresponding wavelength.

The extracted spectra require the proper conversion from pixel-to-wavelength as shown in the final steps of Fig. 10. Spectral features of known absorption or emission lines are identified to build a relationship between pixel location and wavelength.

3.1 The Grating Equation

A diffraction grating separates the incident light into wavelengths due to constructive interference and is represented by the grating equation in Equation (3):

$$\sin \theta_m = \sin \theta + m \frac{\lambda}{D} \quad (3)$$

where D is the line spacing of the grating, θ is the angle of the incident plane corresponding to the 0th order, θ_m is the angle of the incident plane corresponding to the m^{th} order, m is the order number, and λ is the wavelength [9]. This is shown schematically in Fig. 11.

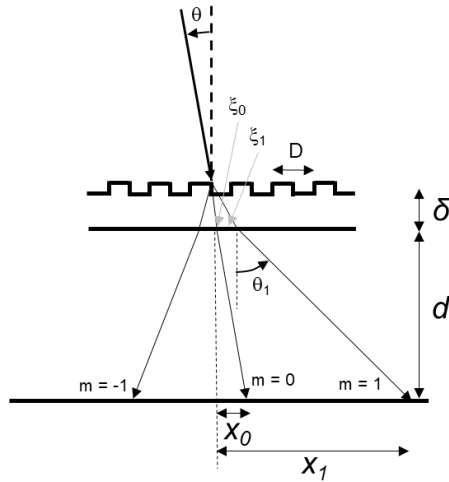


Fig. 11. Schematic of grating equation definitions.

Solving Equation (3) for wavelength yields Equation (4):

$$\lambda = \left(\frac{D \sin \theta_m}{m} \right) + \left(\frac{-D \sin \theta}{m} \right). \quad (4)$$

Using the small angle approximation and distance definitions displayed in Fig. 11 such that $\sin \theta = (x_0 - \xi_0)/d$ and $\sin \theta_m = (x_m - \xi_m)/d$, and defining $\Delta pixels = (x_m - x_0)/s$ where s is the size of a pixel, Equation (4) can be rearranged into Equation (5):

$$\lambda = \left(\frac{D}{dsm} \right) \times \Delta pixels + \left(\frac{-D(\xi_m - \xi_0)}{dm} \right). \quad (5)$$

Equation (5) represents a linear relationship and can be simplified to Equation (6):

$$\lambda = m \times \Delta pixels + b \quad (6)$$

where m is now the linear fit's slope (nm per pixel where wavelength is measured in nm), $\Delta pixels$ is the number of pixels between the 0th order and the spectral feature in the 1st order, and b is the calculated offset in nm. Fig. 12 and Fig. 13 show two samples of the pixel-to-wavelength calibration for two different stars, an A-type main sequence star and a Wolf-Rayet emission-line star, respectively. For Fig. 12, the resulting slope and offset are $m = 1.0415$ nm/pix and $b = 4.6878$ nm. For Fig. 13, the resulting slope and offset are $m = 1.0449$ nm/pix and $b = 0.5118$ nm.

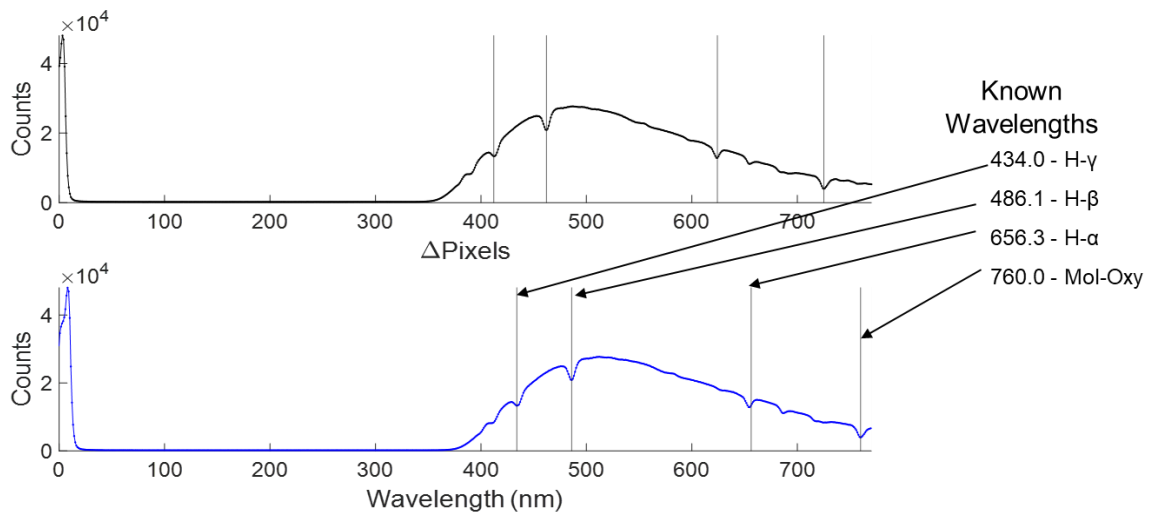


Fig. 12. Vega (A-type main sequence star) spectrum as observed from FTN site OJC.

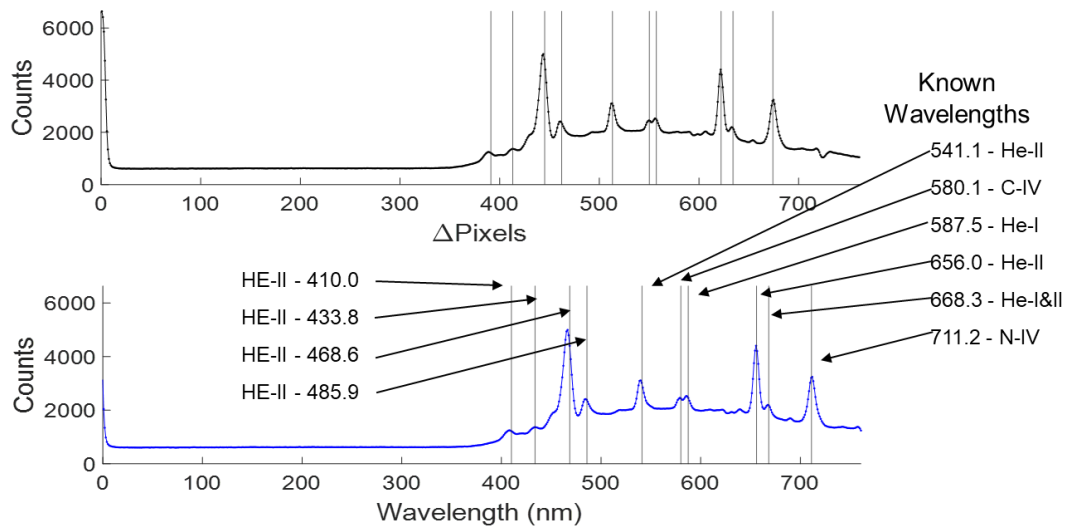


Fig. 13. HD192163 (Wolf-Rayet star) spectrum from FTN site OJC.

3.2 Kwee-van Woerden Method for Subpixel Resolution

Previously, the Δ pixels value corresponding to a spectral feature was simply based on the local maximum or minimum (depending on if it was an emission or absorption feature) pixel value [3]. However, this can be improved by implementing a method to determine the line centers to a sub-pixel resolution. We used the Kwee-van Woerden method to interpolate the data to find a more accurate maximum/minimum of each feature in the spectra [10]. The initial local minimum or maximum pixel value was found through simple identification and serves as an initial axis of reflection. The points directly left and right of the axis were combined to find a difference. This process was repeated for points two to the left and two to the right. These two difference values were added together in quadrature, assigning a single value for this initial axis of reflection. The axis was then shifted one pixel to the left and right of the starting point, and the calculations were repeated. With three values across three points (centered on

the original data's minimum or maximum), the A and B coefficients of the resulting quadratic fit are calculated, and the exact minimum of the interpolated curve is found with Equation (7):

$$x = \frac{2A}{B} \quad (7)$$

where x is the pixel value of the spectral feature center. These improved line centers can be used to calculate a more accurate slope and offset. Applying this method not only provides a more accurate pixel-to-wavelength relationship but also allows automation of a critical part of the spectral pipeline. As long as the algorithm finds the local minima/maxima, the resulting x -values will always be the same, as opposed to the previous method of manually identifying the local minima/maxima. An example of the interpolated pixel value is shown in Fig. 14.

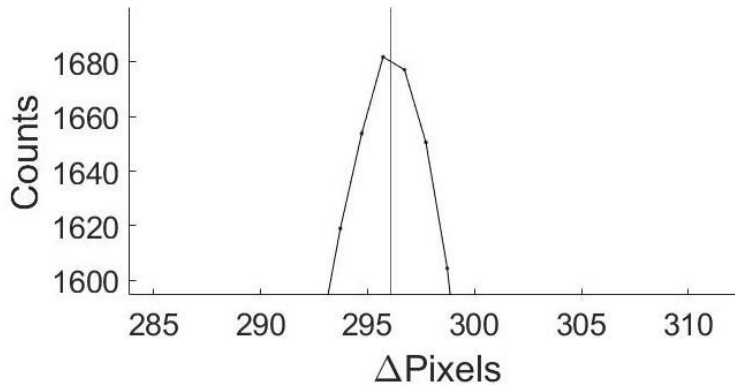


Fig. 14. The Kwee-van Woerden method applied to data taken from the USAFA-16 telescope of the FTN with a vertical line at the calculated spectral center.

Using the Kwee-van Woerden method to determine spectral feature pixel centers aimed to provide a more accurate pixel center which would eventually lead to a more accurate wavelength of each feature within the data. The resulting pixel-to-wavelength conversion is compared directly for the Wolf-Rayet star HD4004 collected at CMU. HD 4004 has five prominent emission features with the results from the original pixel-to-wavelength formulation and the Kwee-van Woerden formulation shown in Table 2. As expected, the sub-pixel resolution realized by the Kwee-van Woerden method provided a wavelength closer to the theoretical value than the original formulation.

Table 2. Difference in Estimated Values of HD4004 Emission Lines from Actual Values

HD 4004 from CMU	468.60 nm	541.10 nm	580.80 nm	656.00 nm	711.50 nm
Original (local max) m = 1.5888 ± 0.0103 b = -2.48 ± 3.90	-1.23	0.94	0.96	0.44	-1.04
KvW method m = 1.5847 ± 0.0047 b = -1.10 ± 1.78	-0.60	0.68	0.24	-0.01	-0.31

3.3 Pixel-to-Wavelength Results

Table 3 details the resulting calibration for various FTN sites using the new sub-pixel spectral feature determination. These values represent the weighted mean of multiple calibration stars per site on the date(s) specified. The calibrations for FLC, MMO, and OJC are new to this paper, while the other calibrations for CMU, NJC and USAFA-

16 were redone from what was previously reported to use the new method and to account for the correction of the expected wavelength of the molecular oxygen atmospheric absorption feature used as a calibration feature for A-type stars. Note that whereas the calibration at CMU did not change very much from 2021 to 2022, the calibration at NJC changed significantly corresponding to a replacement of the site’s CCD camera with the same model which occurred between the two dates. According to Equation (5), the only parameter that could account for the change in slope is the distance between the grating and the CCD focal plane where the new distance is about 10% larger than the original distance. Also note that the diffraction grating at OJC is not the standard grating used in the other FTN sites but rather 150 lines/mm, thus producing a different dispersion (about 1 nm per pixel).

Table 3. FTN Pixel-to-Wavelength Calibrations

Site	Date(s)	m “slope” (nm/pix)	b “offset” (nm)
CMU	2021-01-27	1.5839 ± 0.0010	-5.6 ± 0.4
CMU	2022-02-08/14	1.5914 ± 0.0016	-4.8 ± 0.6
FLC	2021-11-18	1.5574 ± 0.0026	5.6 ± 1.0
MMO	2021-12-04	1.5477 ± 0.0031	10.9 ± 1.2
NJC	2021-03-03	1.5698 ± 0.0028	3.9 ± 1.1
NJC	2022-02-08	1.4311 ± 0.0024	1.1 ± 1.0
OJC	2021-12-03	1.0486 ± 0.0014	2.5 ± 0.8
USAFA-16	2022-02-13	1.5990 ± 0.0068	11.8 ± 1.8

4. EXTINCTION CORRECTION

Atmospheric extinction refers to the absorption of light by the atmosphere and depends on the position of the star or object in the sky as observed by the particular sensor site. In order to compare the spectra of different objects, it is necessary to first account for this atmospheric extinction.

4.1 Atmospheric Extinction Theory

The full derivation of the extinction theory can be found in the Appendix. The result of this derivation—Equation (44)—is repeated in Equation (8):

$$\ln(F_\lambda) = \frac{-k_\lambda}{2.5 \log_{10}(e)} X + \ln(F_{\lambda_0}). \quad (8)$$

The next step is to solve for the extinction coefficient (k_λ).

4.2 Solving for the Extinction Coefficient (k_λ)

We now solve for the extinction coefficient. Equation (8) may be mapped to the slope-intercept expression, as illustrated in Fig. 15.

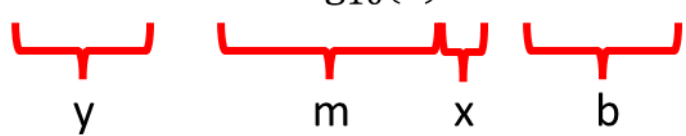
$$\ln(F_\lambda) = \frac{-k_\lambda}{2.5 \log_{10}(e)} X + \ln(F_{\lambda_0})$$


Fig. 15. Mapping of slope-intercept expression to the equation used to solve for the extinction coefficient.

The next step is to solve for the best-fit-line from the known values (data), $\ln(F_\lambda)$ and X . This will determine the slope, $\frac{-k_\lambda}{2.5 \log_{10}(e)}$. Solving for the best-fit-line is shown graphically in Fig. 16 for a single wavelength bin or per-unit wavelength.

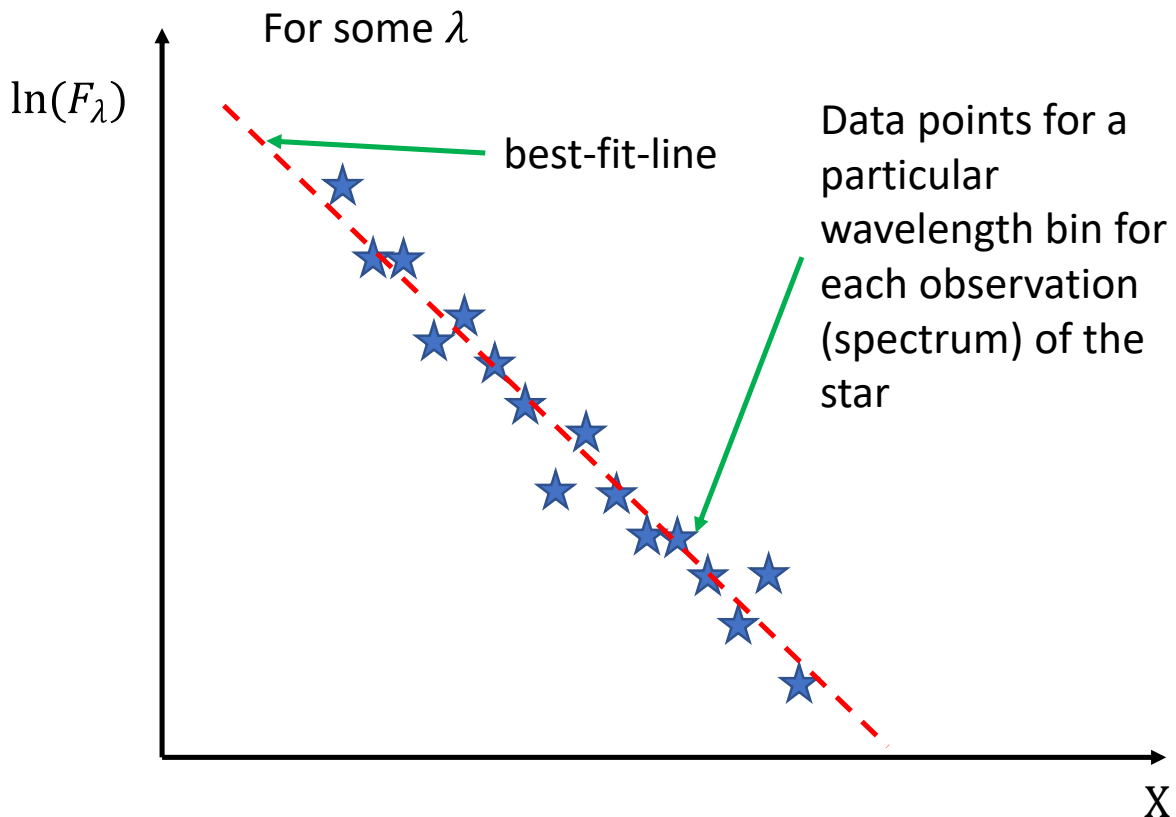


Fig. 16. Notional example of fitting a best-fit-line to the data in a particular wavelength bin of a spectroscopic standard star to solve for the extinction coefficient of that wavelength bin.

This process needs to be repeated for each wavelength bin to solve k_λ for all wavelength bins. This process yields an array of values for k_λ . Now that we have solved for the extinction coefficient per unit wavelength, k_λ , and we know the airmass based on the pointing of the telescope during the observation, X , we can solve for the instrumental flux above the atmosphere per unit wavelength, using Equation (42). With the extinction coefficient per unit wavelength, k_λ , an additional visualization illustrates how the extinction changes as a function of wavelength. Due to Rayleigh

scattering, the visualization shows that the extinction generally decreases as wavelength increases, notionally shown in Fig. 17.

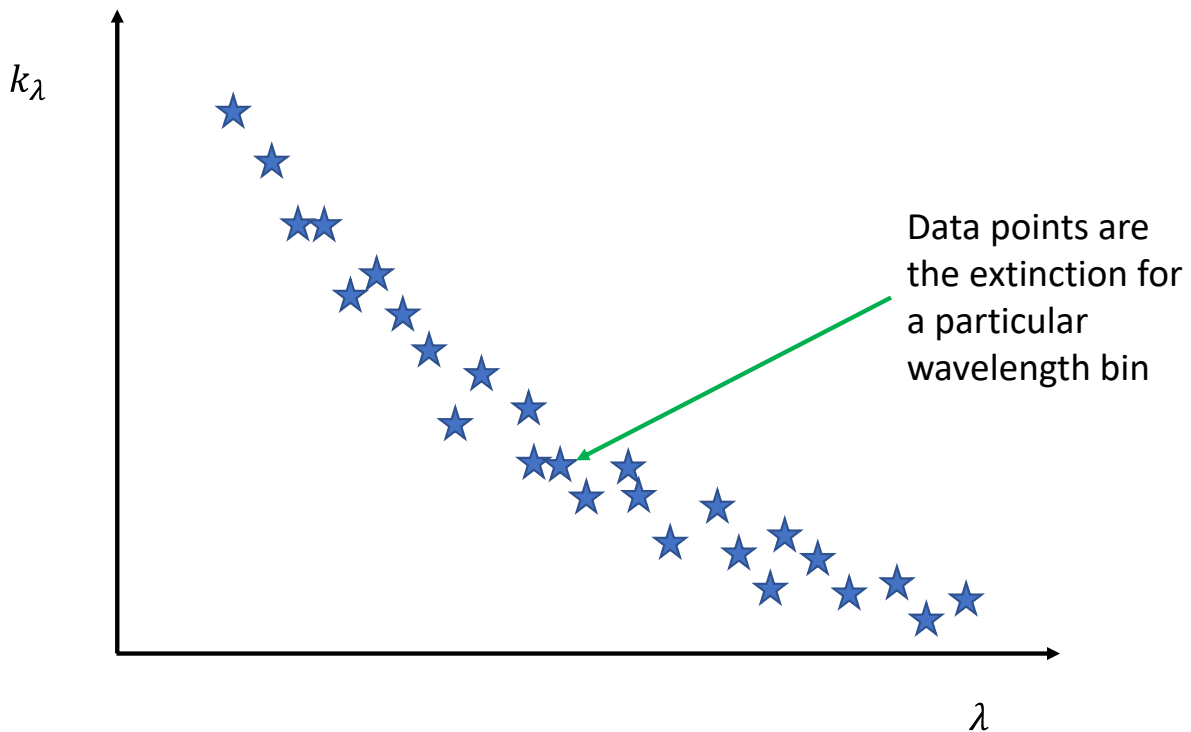


Fig. 17. Notional example showing the extinction coefficient for many wavelength bins and the expected behavior of a decreasing extinction coefficient with increasing wavelength.

4.3 Atmospheric Extinction Results for FTN Site

As with photometry, the atmospheric extinction as a function of wavelength for slitless spectroscopy can be determined by observing the same star over the course of a night at different airmasses. Two stars were observed from the FTN site CMU on 2022 Jun 08: HD95241 and HD128998. Fig. 18 displays all the resulting spectra for both stars.

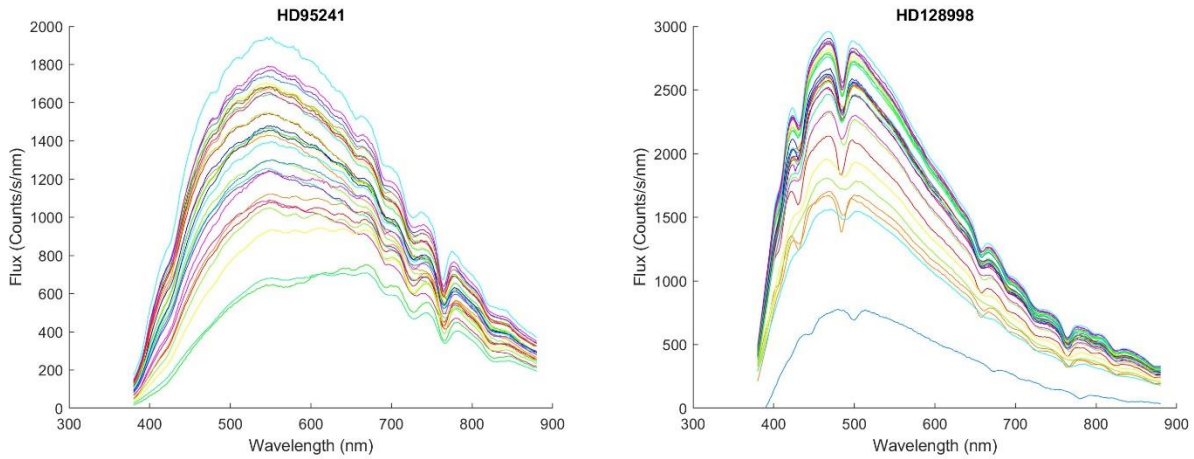


Fig. 18. All spectra (counts/sec vs. wavelength) for extinction stars (HD95241 (left) and HD128998 (right)).

The instrumental magnitude ($2.5 \times \log_{10}$ of the flux in counts/s/nm) as a function of airmass was examined for each wavelength between 380 nm and 880 nm, with the resulting slope corresponding to the atmospheric extinction coefficient at that wavelength. Fig. 19 shows a sample of the instrumental magnitude versus airmass plot for five different wavelengths, while Fig. 20 shows the resulting extinction coefficient as a function of wavelength (extinction curve). Note that not all of the values are used in calculating the extinction. Some spectra were determined to be affected by clouds, and airmasses above 2.5 were not considered. These are shown as x's in Fig. 19.

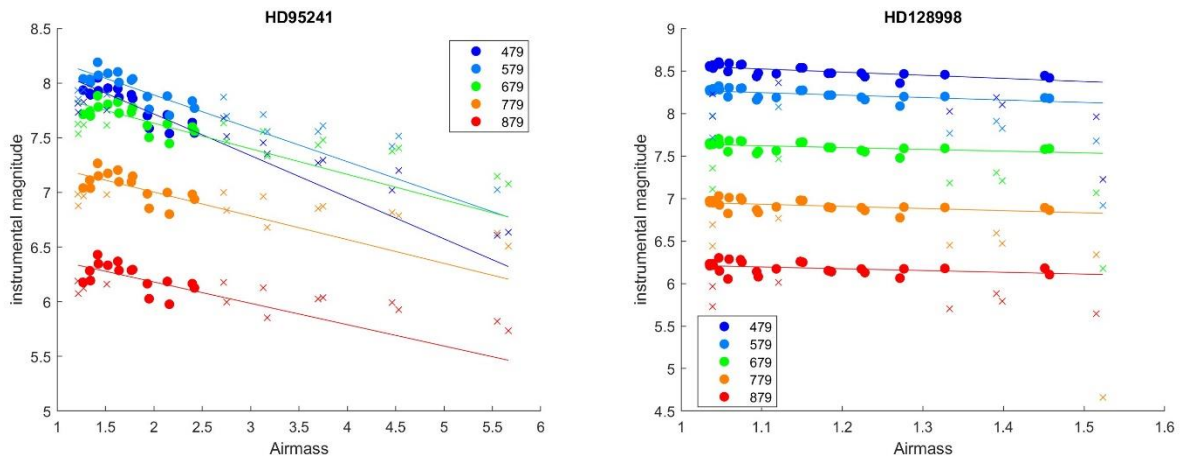


Fig. 19. $2.5 \log_{10}(\text{Flux})$ as function of airmass for five select wavelengths for HD95241 (left) and HD128998 (right).

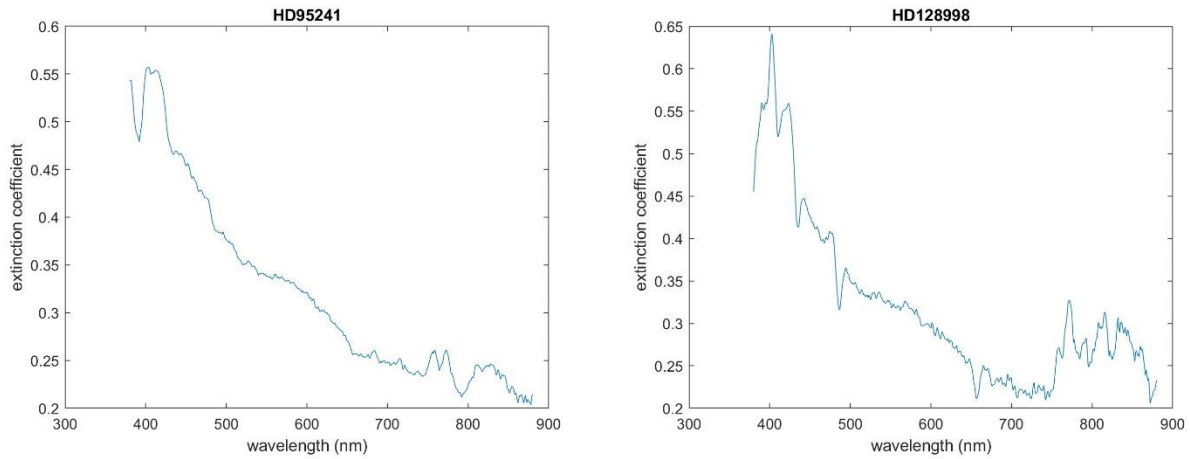


Fig. 20. Resulting extinction as function of wavelength for HD95241 (left) and HD128998 (right).

The two extinction curves were combined and smoothed using a moving mean of 100 nm resulting in the final extinction curve to be used to correct for atmospheric extinction of future spectra. This final plot is shown in Fig. 21.

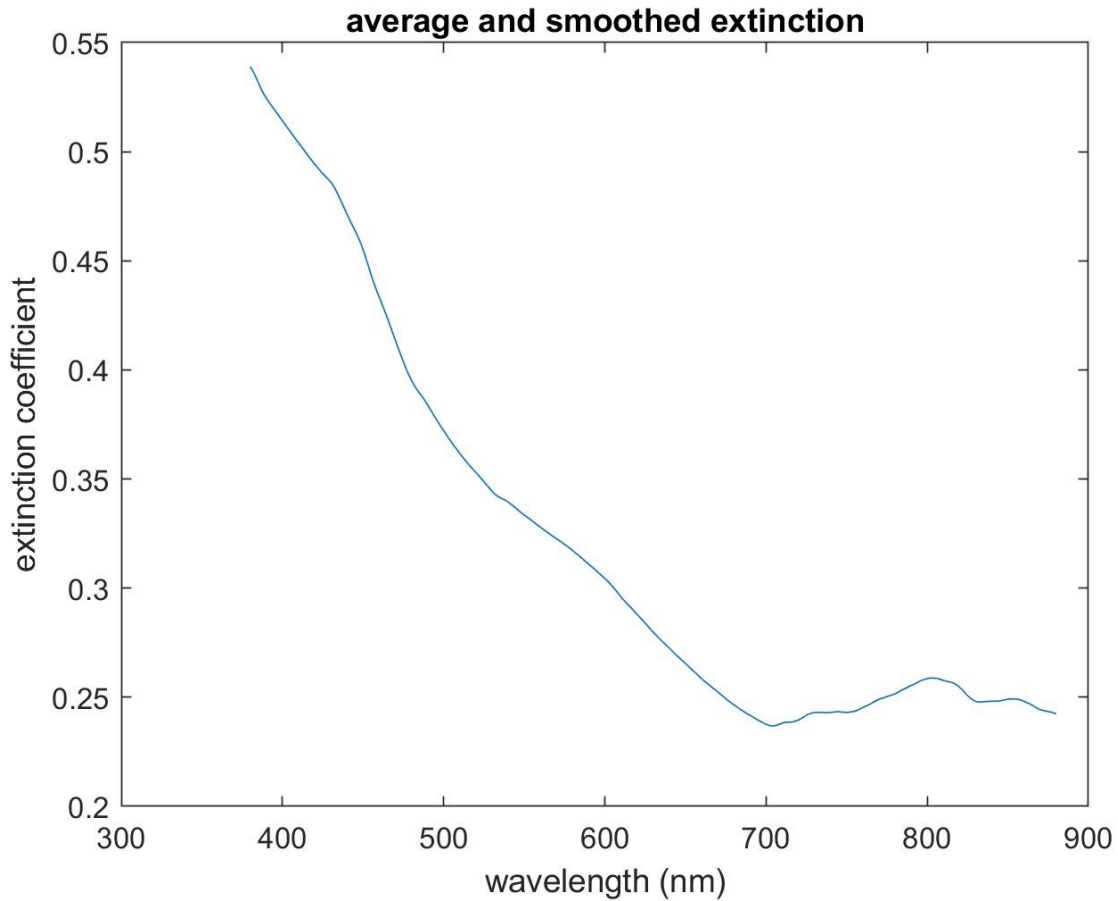


Fig. 21. Averaged and smoothed extinction vs. wavelength for CMU.

5. SOLAR ANALOG NORMALIZATION

Twenty-four solar-type stars between the spectral types of F2V and K2V were observed from the FTN site CMU on 2022 June 08 for the purposes of solar analog normalization (this section) and a solar analog analysis (Section 7). In our analysis in Section 7, several stars were found to be misclassified and removed for the star list. The four stars closest to the Sun’s spectral type (G2V) are shown in Table 4. Note that the stars in Table 4 are a subset of the stars in Table 5 of Section 7.

Table 4. List of Stars Used to Create the Average Solar Analog

Star	Spectra Type	Quality	Bibcode
HD106421	G3V	C	1997JApA...18...161Y
HD126053	G1.5V	C	2003AJ...126...2048G
HD150933	G2V	C	~
HD168009	G1V	C	2003AJ...126...2048G

These stars were used to calculate the average solar analog. Fig. 22 shows the spectra of these four stars, along with the average solar analog. This will represent the average solar analog used for solar analog normalization in Section 6, as well as the solar analog analysis in Section 7.

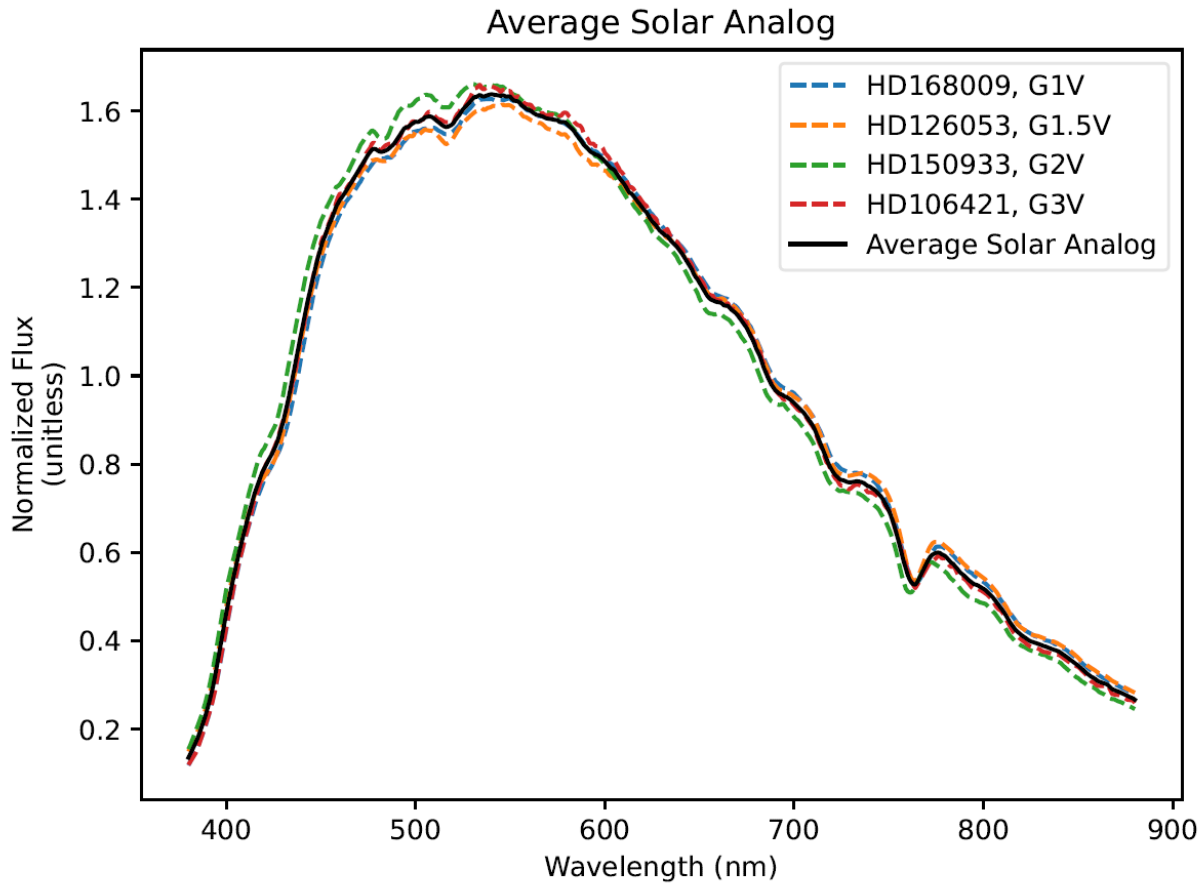


Fig. 22. Average solar analog spectrum.

To normalize the spectrum of an RSO to a solar analog, the RSO spectrum is divided by the average solar analog spectrum. The effect of the processing pipeline steps on the spectra of DTV-10 is discussed in the following section. This process, in theory, removes the solar component of the shape of the reflectance spectra, leaving only the satellite component.

6. DTV-10 SPECTRA

Finally, during the same night as the extinction and solar analog star observations, the GEO satellite DTV-10 was observed. The collections were generally low Signal-to-Noise Ratio (SNR). We show one of the spectra with moderate SNR and demonstrate the steps of the processing pipeline and its effect on the spectrum of DTV-10 in Fig. 23. The top panel shows the instrumental flux (blue) and the extinction corrected flux (green). The bottom panel shows the solar normalized flux using the average solar analog spectrum (Fig. 22). It appears that the solar analog normalized DTV-10 spectrum is red; there is a deficit of flux in the blue wavelengths and an excess of flux in the red wavelengths. Overall, the solar analog normalized spectrum of DTV-10, representing the satellite component of the flux observed, is redder than the Sun.

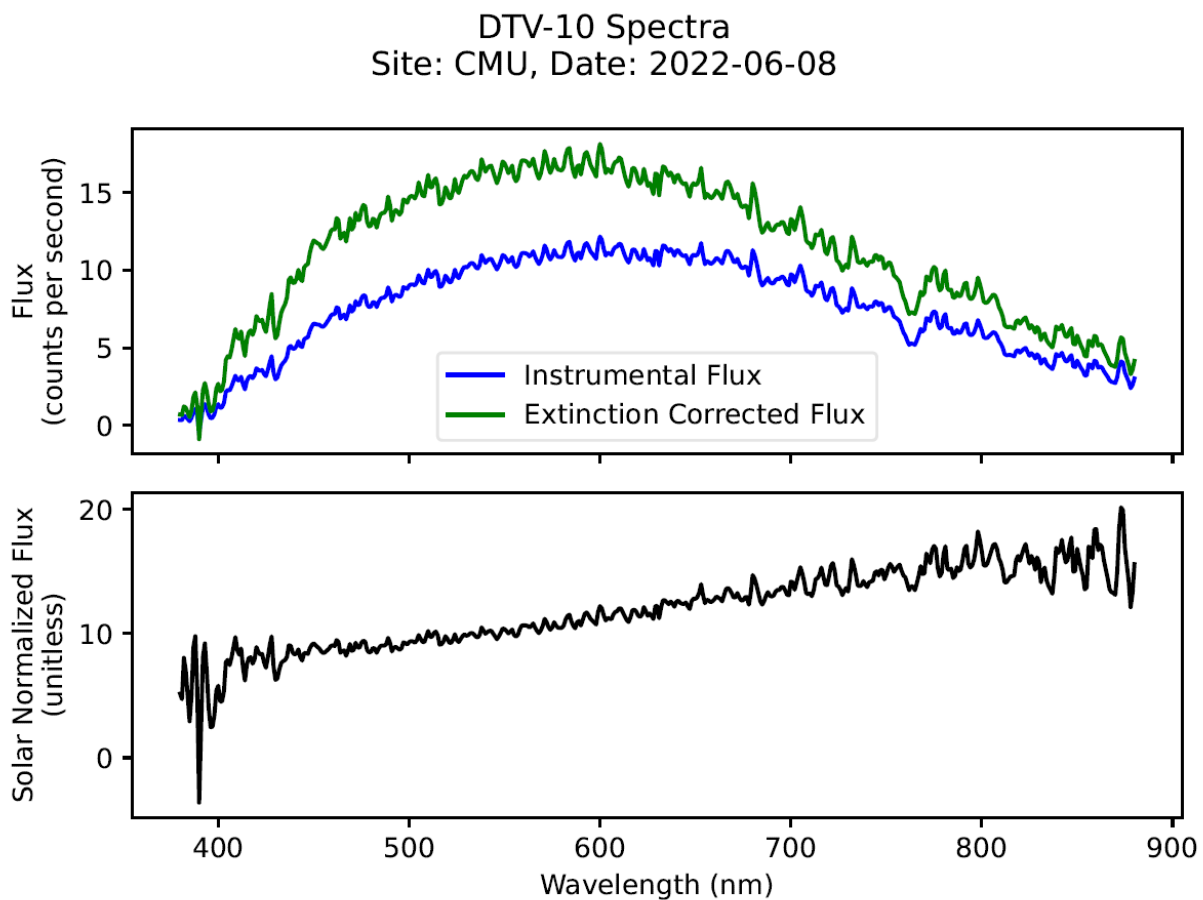


Fig. 23. DTV-10 spectra.

7. SOLAR ANALOG ANALYSIS

Spectroscopy of solar-type stars were collected to perform a solar analog analysis. The solar analog analysis will determine the validity of using stars beyond a spectral subtype of the solar spectral type (G2V) for solar analog normalization. The analysis will determine the error that occurs when using a solar-type star relative to a proper

solar analog. We hope this informs the space domain awareness community about what spectral types are valid to use for solar analog normalization.

For a description of the terms solar-type and solar analog, we refer to [11]. The term solar-type star means stars that are like the Sun. The spectral type range for solar-type stars is given as F8V to K2V by [11]. For this work, we use the spectral type range of F2V to K1V, almost a full spectral type on either side of G2V, and refer to these as solar-type stars. Solar analogs are a subset of solar-type stars. Solar analogs have properties that are similar to the Sun such as temperature (within ~500 K), metallicity (with a factor of two of solar), within one magnitude of the zero-age main sequence (still burning hydrogen), and no close companion. Since many of these properties are not known for stars, we use spectral type as a proxy. For our analysis, we define a solar analog as a solar spectral type (G2V) or a subtype from it (G1V or G3V).

Twenty-four solar-type stars between the spectral types of F2V and K2V were observed from the FTN site CMU on 2022 June 08. The details of these stars are listed in Table 5. The quality (A = best to E = worst) and bibcode are those listed for each star in the SIMBAD¹ database. Note that the stars in Table 4 are a subset of the stars in Table 5. The earliest spectral type observed is F2V, and the latest spectral type observed is K0.5V. Through our analysis, we discovered that HD152306 (G2V) and HD120787 (G3V) had their spectral types misclassified, being more likely K-type stars. These two stars were removed from the star list, leaving 22 stars for the solar analog analysis.

¹ <http://simbad.cds.unistra.fr/simbad/sim-fbasic>

Table 5. List of Solar-Type Stars

Star	Spectra Type	Quality	Bibcode
HD95241	F9V	D	1996A&A...314...191G
HD99285	F2V	C	1989ApJS...69...301G
HD99373	F5.5IV-V	C	2001AJ...121...2148G
HD100563	F5.5V	C	2006AJ...132...161G
HD101501	G8V	B	1989ApJS...71...245K
HD103799	F6V	D	2009MNRAS...396...1895C
HD106421	G3V	C	1997JApA...18...161Y
HD110897	F9V Fe-0.3	C	2003AJ...126...2048G
HD111395	G5V	E	~
HD117043	G6V	C	2018ApJS...238...29P
HD117176	G4Va	B	1989ApJS...71...245K
HD120787	G3V	D	~
HD126053	G1.5V	C	2003AJ...126...2048G
HD126081	K0V	C	~
HD127334	G5V CH0.3	C	2003AJ...125...984M
HD131511	K0.5V	C	1989ApJS...71...245K
HD134044	F8V	D	~
HD140667	G0V	C	~
HD142267	G1V Fe-1	B	1989ApJS...71...245K
HD150933	G2V	C	~
HD152306	G2V	D	~
HD153226	K0V	C	~
HD157373	F4V	C	~
HD168009	G1V	C	2003AJ...126...2048G

The remaining spectral plots of this section are color coded by spectral type: purple are early spectral types (early F-type stars), and red are later spectral types (early K-type stars), with the spectral types in between filling out the colors of the electro-magnetic spectrum. Late F-type stars are blue, early G-type stars are green, and late G-type stars are yellow and orange.

Fig. 24 shows the instrumental flux (top) and the extinction corrected flux (bottom) for the solar-type stars. The extinction corrected flux is larger than the instrumental flux, as expected. Fig. 25 shows the same as the bottom of Fig. 24 but now normalized to an average of one. The hotter stars (earlier spectral types) have their flux peak at shorter wavelengths than the cooler stars (later spectral types), consistent with the Wien displacement law [12]. These normalized solar-type stars will be used throughout this section.

Solar-Type Stars

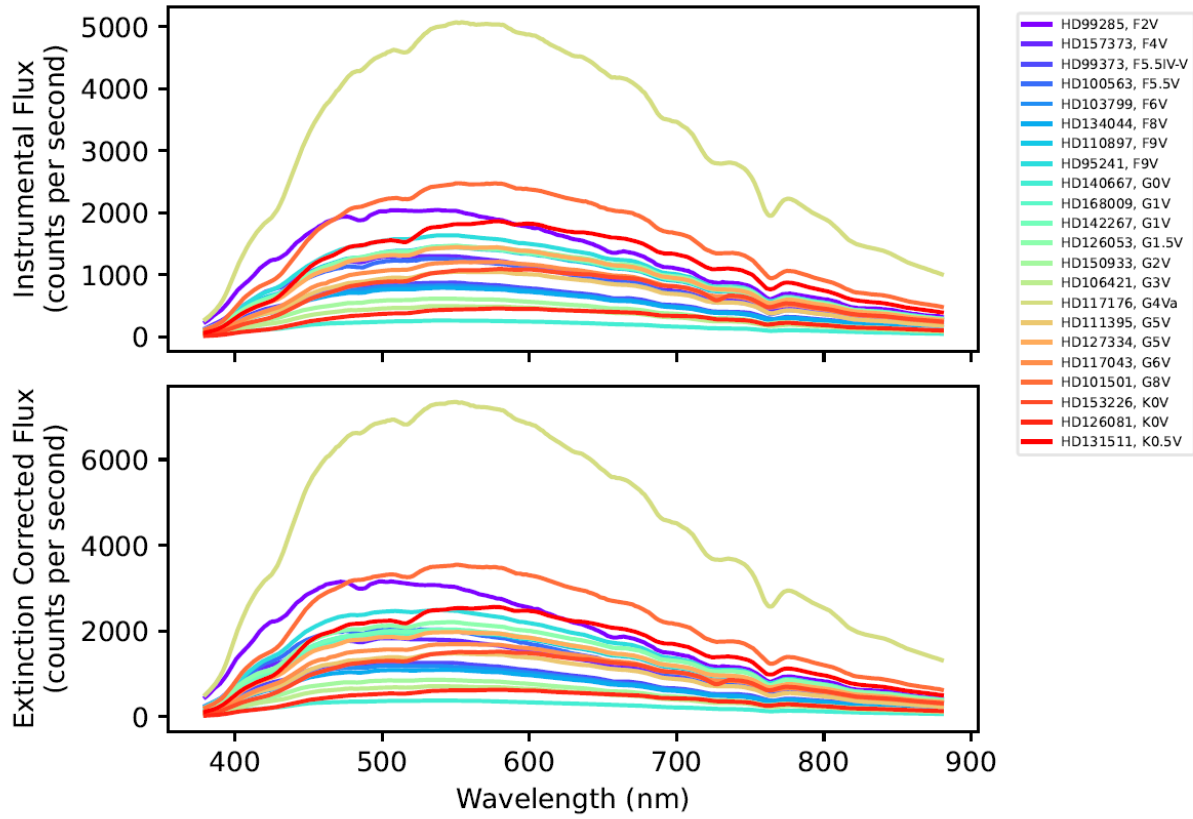


Fig. 24. Instrumental flux (top) and extinction corrected flux (bottom) for all solar-type stars.

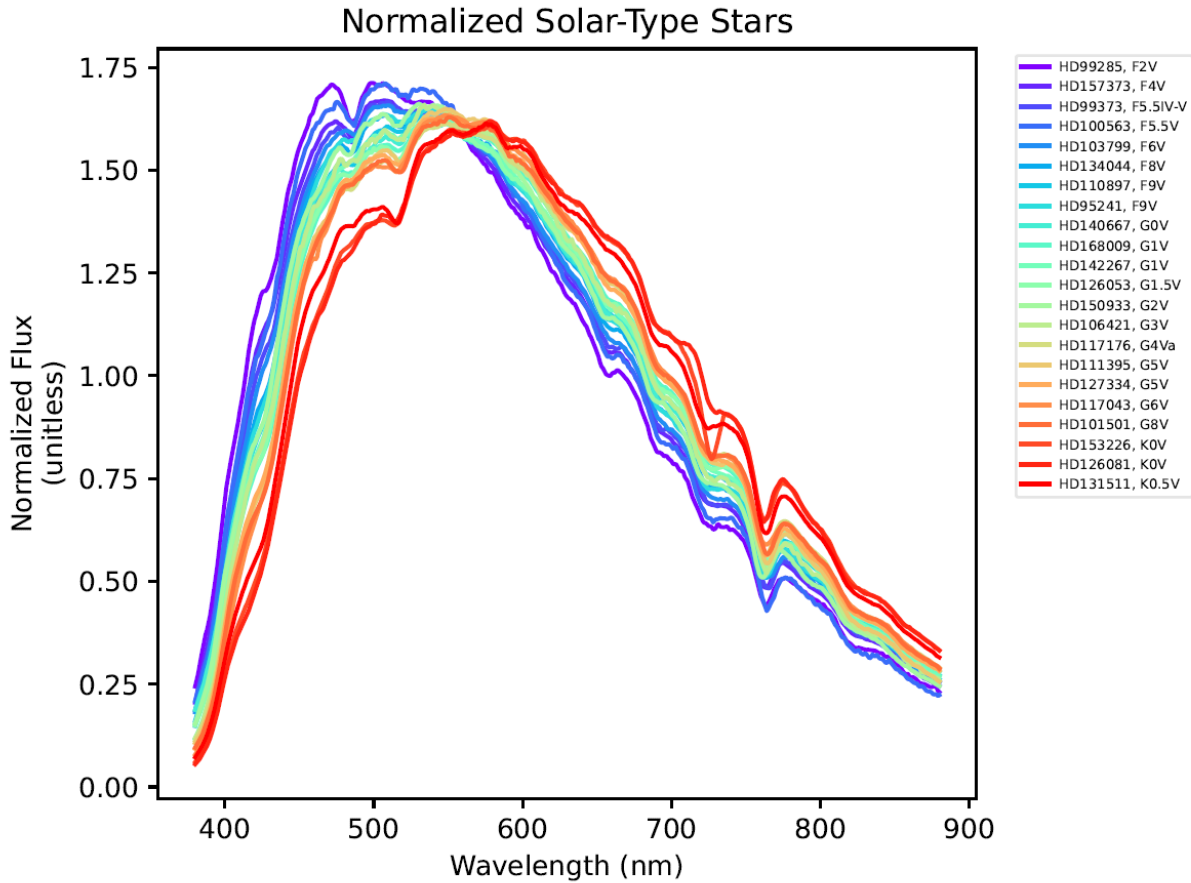


Fig. 25. Normalized extinction corrected flux as function of wavelength for solar-type stars.

If the average solar analog is applied to the solar-type stars in Fig. 25, the result is shown in Fig. 26. Note that the stars hotter than the Sun are brighter in blue while fainter in red, while the stars cooler than the Sun are brighter in red while fainter in blue. The stars with temperatures closest to the Sun have a nearly flat profile in this solar analog comparison.

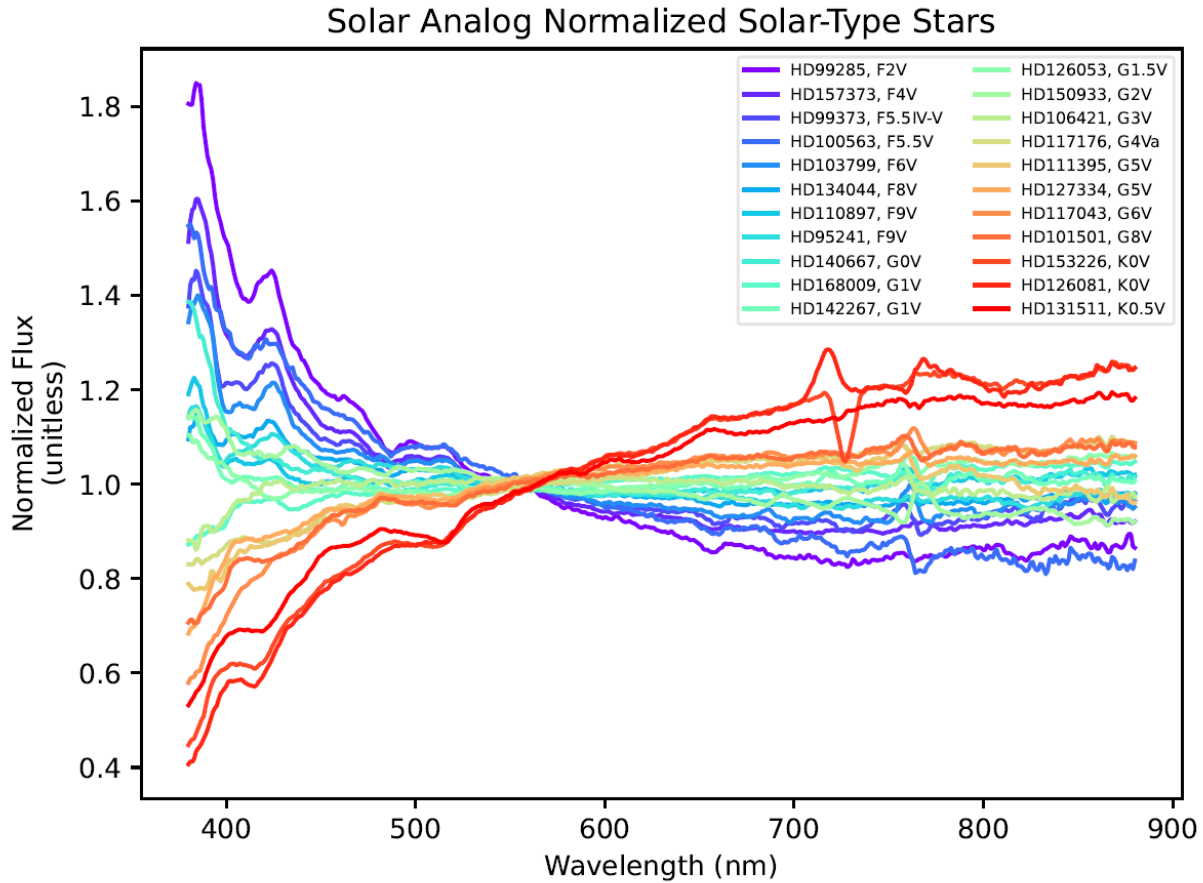


Fig. 26. Solar-type stars normalized using the average solar analog spectrum.

We use the chi-squared expression from [13] to compare the spectra. In [13], they used the chi-squared expression as a metric to compare a measured spectrum to a synthesized binary to help identify a peculiar spectrum as an unresolved binary via spectral template matching. We use this same chi-squared expression but adapt it for our purposes, as a metric to compare spectra. This method has been used to determine the spectral type of a spectrum [14]. The expression in Equation (9) is used to calculate chi-squared for the comparison between spectra:

$$\chi^2 = \sum_{\lambda} [f_{\lambda}(Solar) - f_{\lambda}(Comparison)]^2 / f_{\lambda}(Solar). \quad (9)$$

Fig. 27 shows the chi-squared comparison of the solar-type spectral relative to the average solar analog. Here, $f_{\lambda}(Solar)$ is the flux of the average solar analog spectrum, and $f_{\lambda}(Comparison)$ is the flux of the comparison spectrum, the solar-type star spectra. The chi-squared results show that the average solar analog spectrum has a minimum around G1V; it matches a G1V spectral type the best. The chi-squared value increases on either side away from G1V, with a parabola-like behavior.

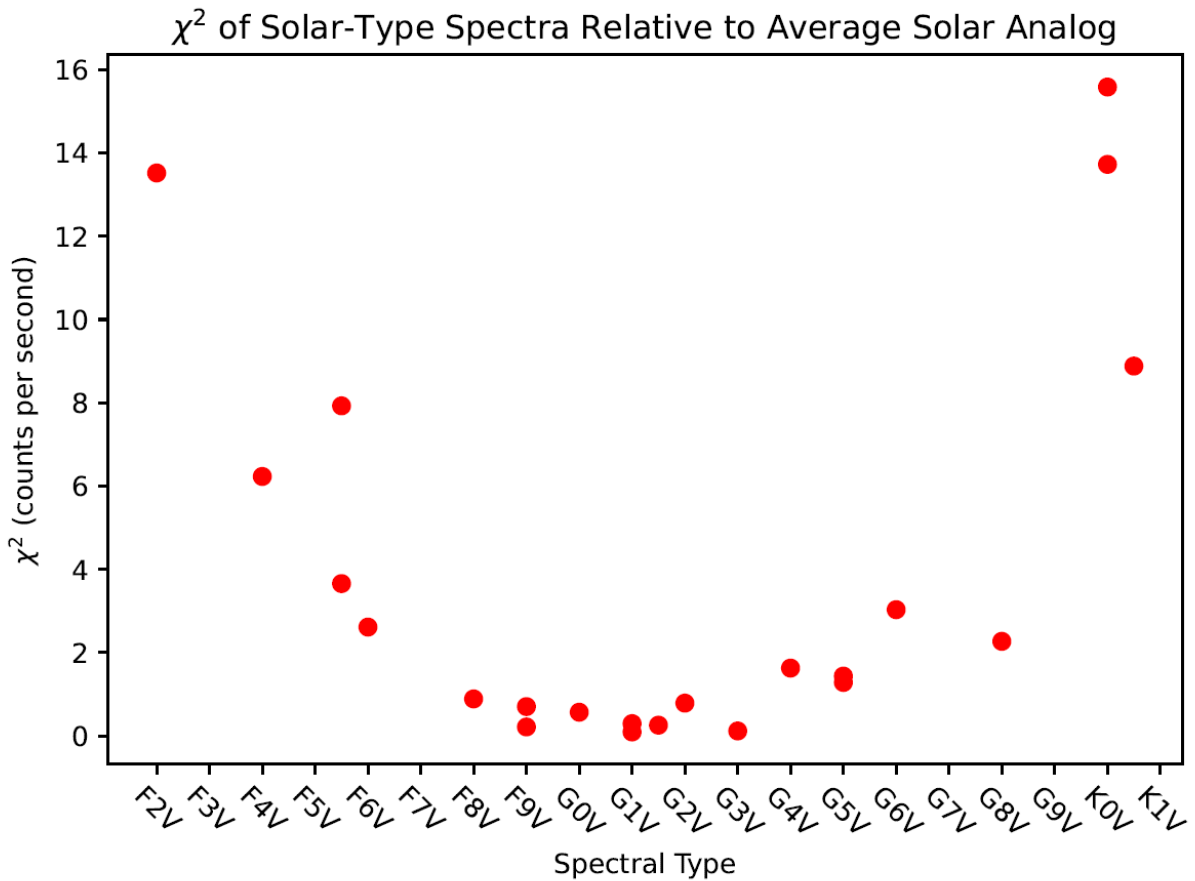


Fig. 27. Chi-squared comparison of solar-type spectra relative to the average solar analog.

Fig. 28 shows the chi-squared comparison of solar-type spectra relative to a G2V (HD150933). The G2V (HD150933) spectrum is included in the analysis and is shown to have a chi-squared value of zero. Note how the chi-squared values have a minimum around F8V or F9V. This indicates that the G2V (HD150933) may be misclassified and may be closer to an F8V or F9V. The chi-squared value for the G3V data point appears to be slightly out of place as well. It is possible this is due to some variation in the G3V spectral type itself, or the spectral type could be slightly misclassified.

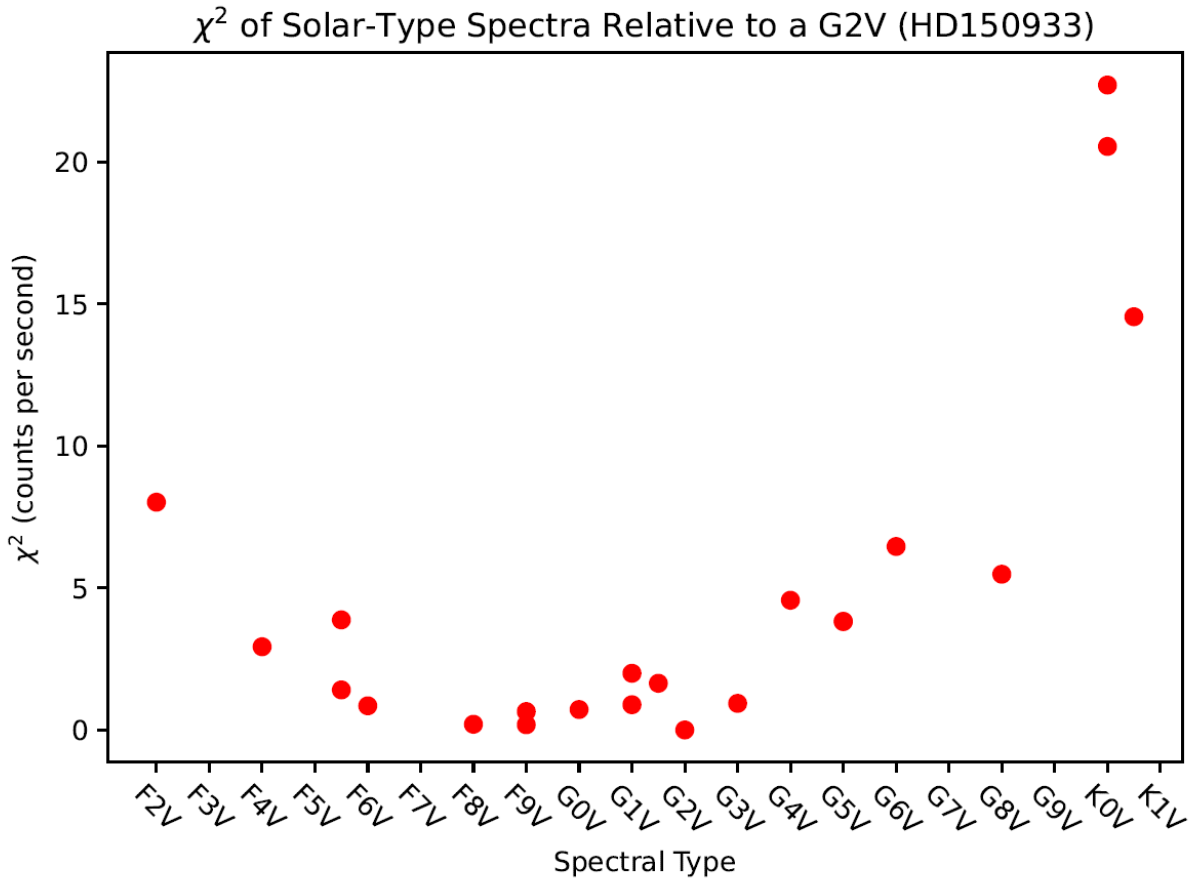


Fig. 28. Chi-squared comparison of solar-type spectra relative to a G2V (HD150933).

Fig. 29 shows the DTV-10 spectrum normalized using the solar-type stars and the average solar analog. Using a spectral type that is earlier than around G2V tends to make the solar normalized spectrum redder, and using a spectral type that is later tends to make the solar normalized spectrum bluer. This is a systematic effect for solar analog normalization that may occur if not using a proper solar analog.

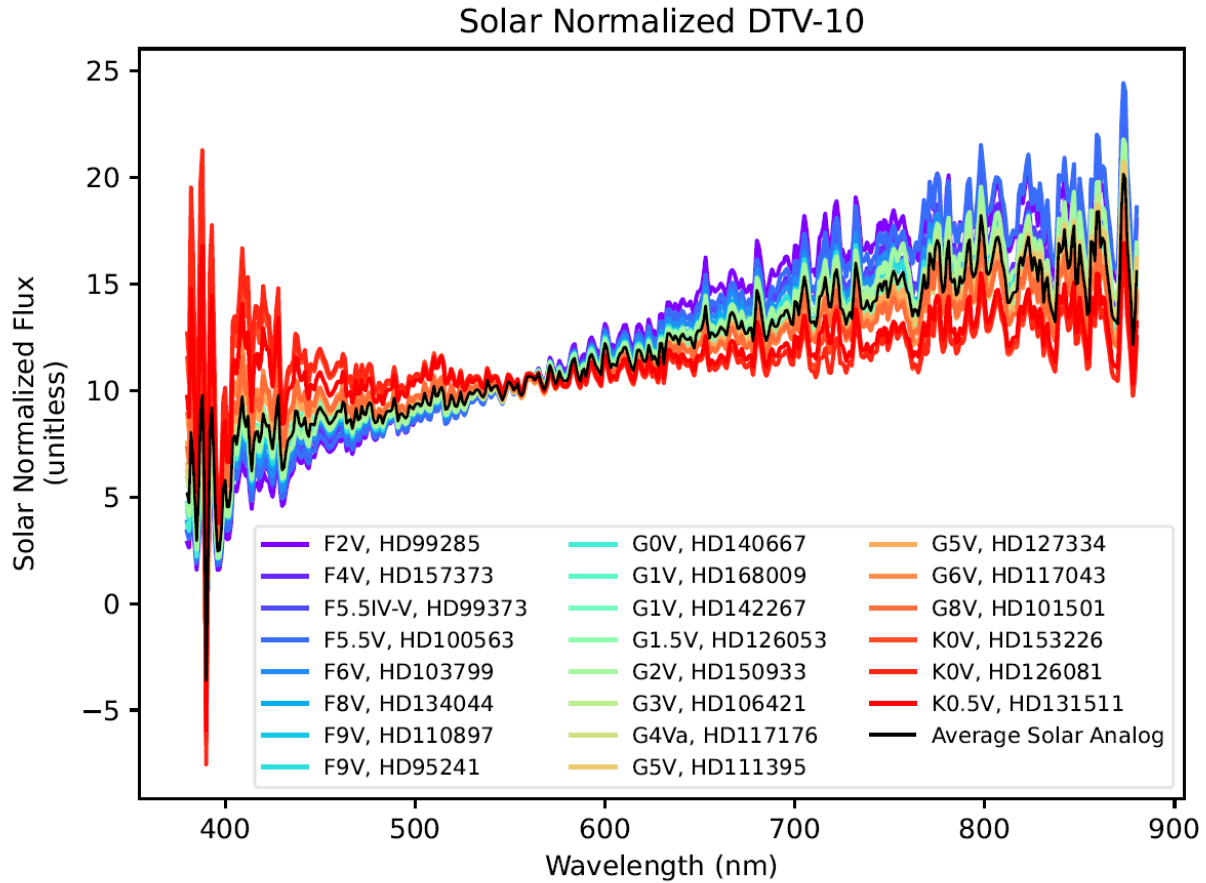


Fig. 29. Solar normalized DTV-10.

We may perform a chi-squared comparison as we did with the solar-type stars but now with the normalized DTV-10 spectrum. Fig. 30 shows a chi-squared comparison of the solar analog normalized DTV-10, normalized using the average solar analog, relative to the DTV-10 spectra normalized using the solar-type stars. In the calculation of chi-squared, $f_{\lambda}(Solar)$ is the flux of DTV-10 normalized using the solar analog spectrum, and $f_{\lambda}(Comparison)$ is the flux of DTV-10 normalized using one of the solar-type stars. These results are similar to Fig. 27 in that the minimum is around G1V; however, the data is a bit flatter around G1V.

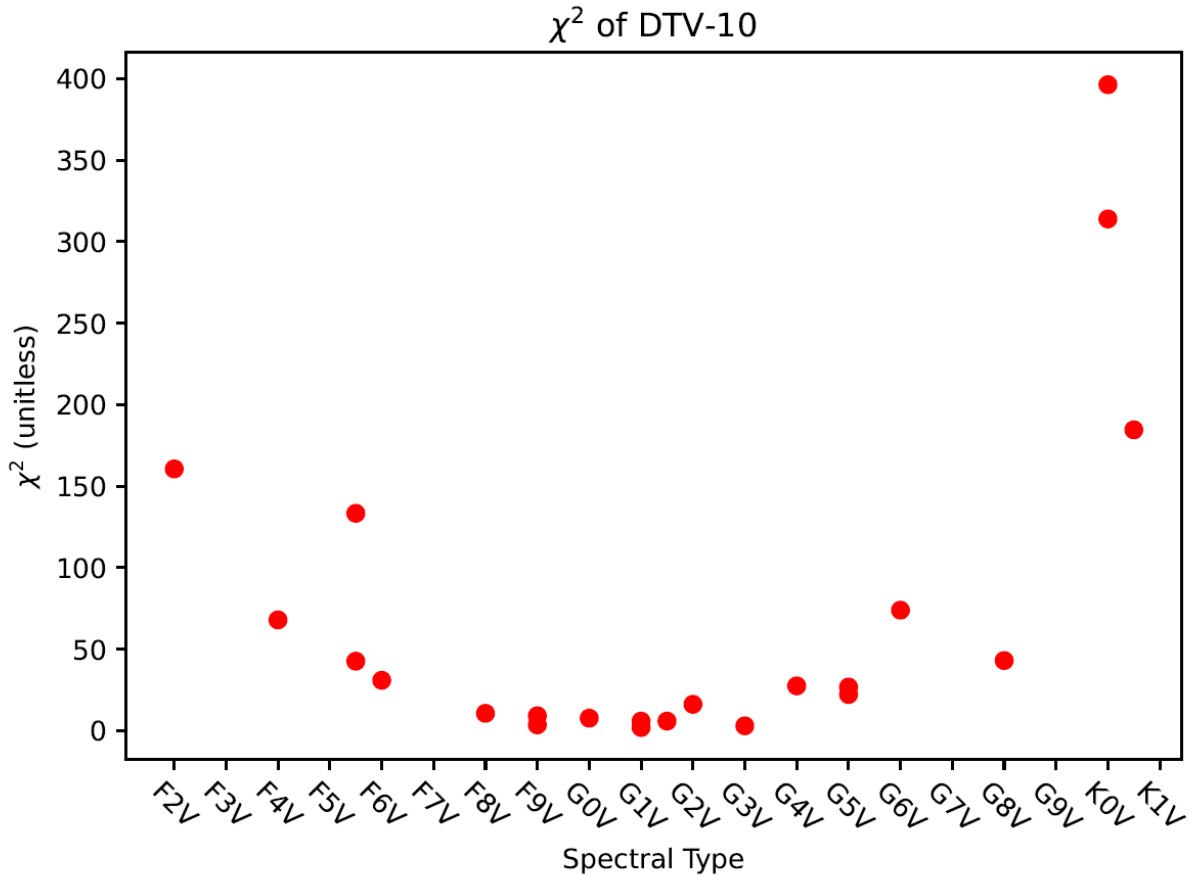


Fig. 30. Chi-squared comparison of solar normalized DTV-10.

Of particular importance is the error introduced for the solar analog normalization process, especially if the spectrum used for normalization is not a proper solar analog. We calculate the percent error between normalization of DTV-10 using the average solar analog and the solar-type stars. This is the error we can expect to have in the solar analog normalized RSO spectrum if we use a particular solar-type star compared to the average solar analog. We define percent error² as Equation (10):

$$\text{Percent Error} = 100 \times |(f_{\lambda}(\text{Solar}) - f_{\lambda}(\text{Comparison}))/f_{\lambda}(\text{Solar})|. \quad (10)$$

We calculate the percent error of the DTV-10 spectrum that is normalized using the average solar analog relative to the DTV-10 spectrum that is normalized using the solar-type stars. Fig. 31 shows the percent error of DTV-10 as a function of wavelength. The percent error becomes very low for most of the stars near 550 to 600 nm. As expected, the spectral types near solar (G2V), depicted as the green lines in the plot, show the lowest percent error, while the earlier (early F-type stars) and later spectral types (early K-type stars) show the largest percent error. Note that the percent error is generally larger for the shorter wavelengths than the longer wavelengths. For spectral types at or close to solar (G2V), depicted as the green lines in the plot, the percent error is small, about 5-10%.

² We use one of the expressions for relative difference from [11], take the absolute value and multiplying by 100. A similar expression for percent error can also be found in [2].

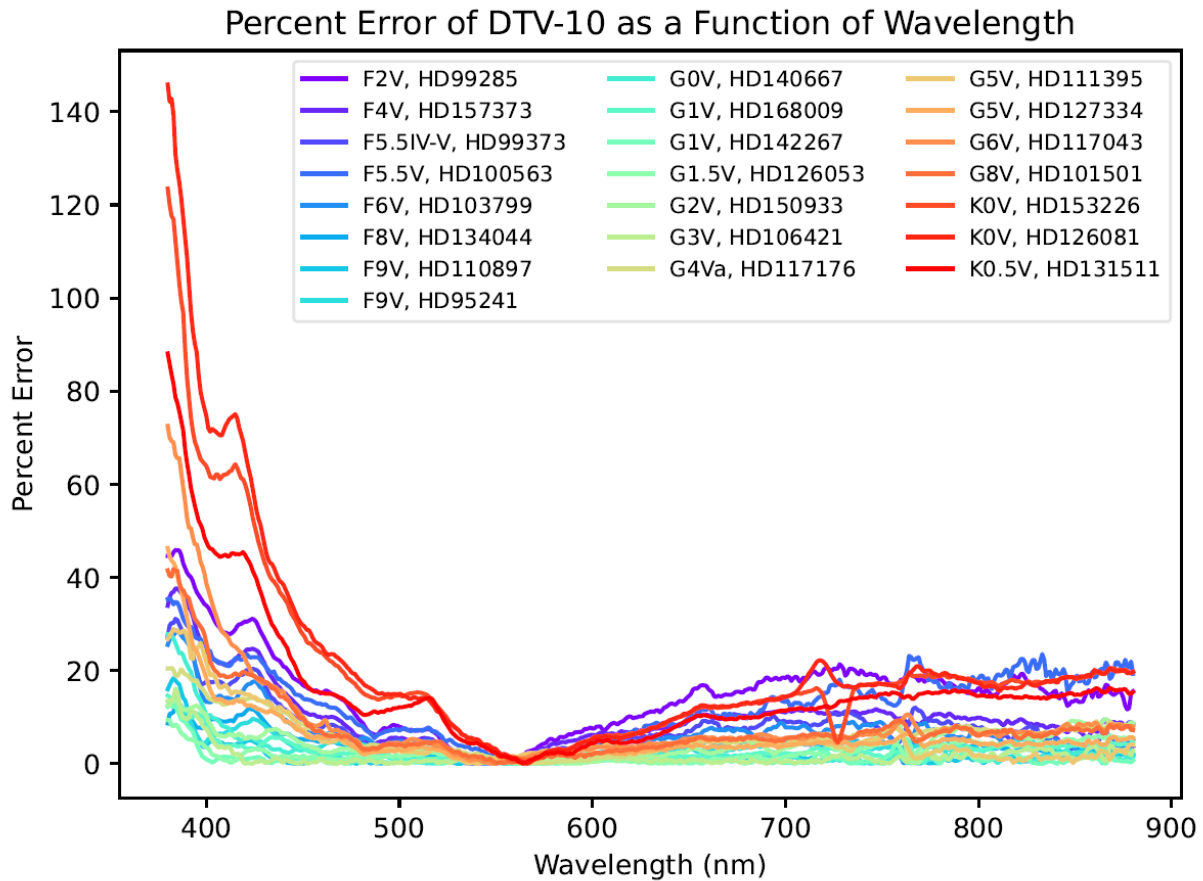


Fig. 31. Percent error of DTV-10 as a function of wavelength.

To provide a more simplistic quantitative result, one that eliminates the dimension of wavelength, we calculate the minimum, maximum, mean, and median of the percent error and show these results as a function of spectral type in Fig. 32. The minimum percent error for all spectral types is very small, around a few percent. The maximum percent error is a minimum around the G1.5 V spectral type, quite large for the early K-type stars, with values exceeding 100%. The maximum percent error for a G1.5V spectral type is still about 10%, with the spectral types nearby having values around 10-20%. There is a jump in maximum percent error for the G0V spectral type, about 30%. Note the asymmetry in the maximum percent error; eight subtypes later than G2V, the K0V has a maximum percent error above 100%, whereas eight subtypes earlier than G2V, the F6V has a maximum percent error of about 30%. The median percent errors are consistent with the mean percent error, with some of the mid to early K-type stars having a median percent error slightly lower than the mean percent error. The median percent error for a G2V and the surrounding spectral types are around a few percent. Note that the median percent error behavior follows that of a shallow parabola, while the maximum percent error behavior follows a sharper parabola; the percent error increases much faster for the maximum percent error compared to the median percent error with deviation from a solar spectral type (G2V).

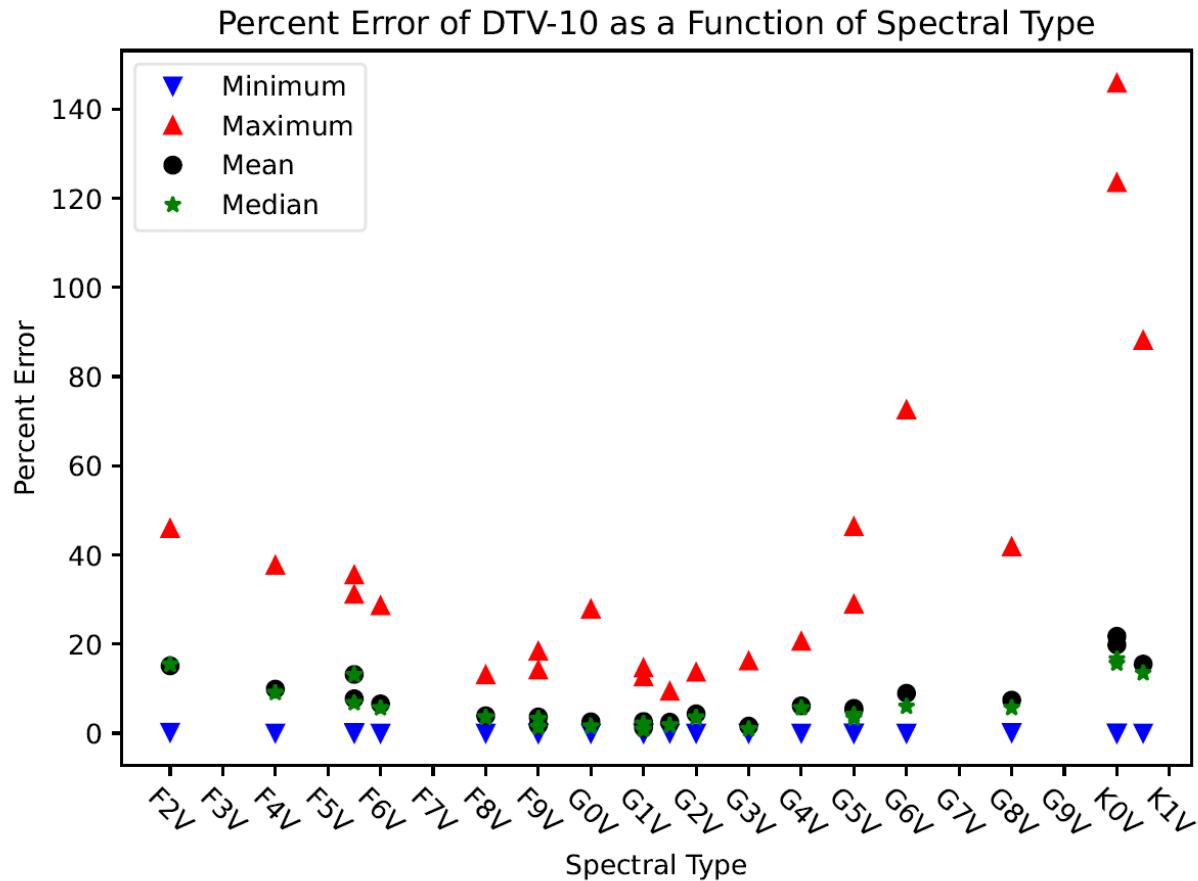


Fig. 32. Percent error of DTV-10 as a function of spectral type.

Data providers calibrating their RSO observations using solar analog normalization need to be cautious with what stars they use for normalization and the error that may occur through either a spectral type being misclassified (e.g., as a G2V) or choosing a star whose spectral type deviates from a solar spectral type (G2V). The solar analog analysis presented here provides a preliminary analysis of solar-type stars and their validity and error in normalizing RSOs. Due to the limited number of solar-type stars observed and some of them being misclassified spectral types, further analysis is warranted. This would include observing a larger number of solar-type stars, such that all of the spectral types from around F2V to K1V are populated, and having multiple stars for each spectral type.

This analysis highlights the danger of using stars that are classified as a solar spectral type (G2V) or close to a solar spectral type (G1V or G3V), where the spectral type is in error. Some type of validation should occur, such as a chi-squared comparison to other solar-type stars, when using a spectrum for solar analog normalization or building an average solar analog spectrum from observations of multiple stars.

8. SUMMARY AND FUTURE WORK

Spectral signatures of artificial satellites can be measured using diffraction gratings. In this paper, we present steps of a spectral image processing pipeline improving on processing code developed by previous cadets which relied heavily on manual settings dependent on telescope and satellite parameters. First, we developed a new method for generating spectroscopic flat-fields that captures both macro- and micro-scale effects, further improving the accuracy of our satellite spectral measurements. Second, we implemented a method to determine spectral features on a sub-pixel level using the Kwee-van Woerden method, resulting in increased precision of the pixel-to-

wavelength calibration. Third, we developed and implemented a procedure to determine the atmospheric extinction for a given night by periodically observing the spectral signature of a standard star throughout the night as its airmass varies. Fourth, we implemented solar analog normalization as a final calibration step. These calibration enhancements were integrated into a new spectroscopic pipeline to process spectral signatures of GEO satellites. Additionally, we performed a solar analog analysis to assess the best spectral type of stars to be used for solar analog normalization in an attempt to constrain what spectral types are valid for this type of calibration. The spectra of solar-type stars (spectral types near G2V) were collected, extinction corrected, used to normalize a GEO satellite, and the resulting solar analog normalized spectra were compared.

Future work includes a major upgrade program to increase the reliability and capability of the FTN. Major upgrades include: 1) a direct-drive mount for faster slew rates, and more accurate pointing and tracking; 2) a large format camera tripling the field-of-view; and 3) dual filter wheels to enable different combinations of filters. Additionally, we are developing various collection plans to examine satellite spectra throughout the year versus just during glint season to both understand the variations we might observe as well as aid in classification schemes using machine-learning techniques.

9. ACKNOWLEDGEMENTS

We want to acknowledge the support of the Air Force Office of Scientific Research. Additionally, this paper is the result of multiple physics senior capstone projects and independent studies at the United States Air Force Academy.

DISCLAIMER: The views expressed in this article are those of the authors and do not necessarily reflect the official policy or position of the United States Air Force Academy, the United States Air Force, the United States Space Force, the Department of Defense, or the U.S. Government.

10. REFERENCES

- [1] D. O. Fulcoly, K. I. Kalamaroff and F. K. Chun, "Determining Basic Satellite Shape from Photometric Light Curves," *Journal of Spacecraft and Rockets*, vol. 49, no. 1, pp. 76-82, 2012.
- [2] A. N. Dunsmore, J. A. Key, R. M. Tucker, E. M. Weld, F. K. Chun and R. D. Tippetts, "Spectral Measurements of Geosynchronous Satellites During Glint Season," *Journal of Spacecraft and Rockets*, vol. 54, no. 2, pp. 349-355, 2017.
- [3] R. D. Tippetts, S. Wakefield, S. Young, I. Ferguson, C. Earp-Pitkins and F. K. Chun, "Slitless spectroscopy of geosynchronous satellites," *Optical Engineering*, vol. 54, no. 10, 2015.
- [4] V. Reddy, A. Battle, T. Campbell, P. Chodas, A. Conrad, D. Engelhart, J. Frith, R. Furfaro, D. Farnocchia, R. Hoffmann, O. Kuhn, D. Monet, N. Pearson, E. Plis, J. Reyes, B. Rothberg, B. Sharkey, J. Sanchez, C. Veillet and R. Wainscoat, "Spectral Characterization of 2020 SO," in *Advanced Maui Optical and Space Surveillance Technologies Conference (AMOS)*, 2021.
- [5] A. Battle, V. Reddy, R. Furfaro, T. Campbell, J. Frith and D. Monet, "A Visible Spectral Atlas of Geostationary Satellites," in *Advanced Maui Optical and Space Surveillance Technologies Conference (AMOS)*, 2021.
- [6] D. Bédard, G. A. Wade, D. Monin and R. Scott, "Spectrometric characterization of geostationary satellites," in *Advanced Maui Optical and Space Surveillance Technologies Conference (AMOS)*, 2012.

- [7] K. Jorgensen, J. Okada, J. Africano, D. Hall, M. Guyote, K. Hamada, G. Stansbery, E. Barker and P. Kervin, "Reflectance Spectra of Human-Made Space Objects," in *Advanced Maui Optical and Space Surveillance Technologies Conference (AMOS)*, 2004.
- [8] F. K. Chun, R. D. Tippets, D. M. Strong, D. J. Della-Rose, D. E. Polsgrove, K. C. Gresham, J. A. Reid, C. P. Christy, M. Korbitz, J. Gray, S. Gartin, D. Coles, R. K. Haaland, R. Walker, J. Workman, J. Mansur, V. Mansur, T. Hancock, J. D. Erdley, T. S. Taylor, R. A. Peters, C. X. Palma, W. Mandeville, S. Bygren, C. Randall, K. Schafer, T. McLaughlin, J. L. N. Castellón, A. C. R. Rivera, H. A. C. Larenas, A. Lambert, M. C. Polo, D. Blair, M. Gargano, J. Devlin, R. Tonello, C. Wiedemann, C. Keschull and E. Stoll, "A New Global Array of Optical Telescopes: The Falcon Telescope Network," *Publications of the Astronomical Society of the Pacific*, vol. 130, no. 991, 2018.
- [9] E. M. Albrecht, E. G. Jensen, K. A. Wilson, A. J. Key, F. K. Chun, N. H. Ruby, D. M. Strong and C. P. Schuetz-Christy, "Photometric and Spectral Calibration of the Falcon Telescope Network," in *Advanced Maui Optical and Space Surveillance Technologies Conference (AMOS)*, 2021.
- [10] K. K. Kwee and H. van Woerden, "A method for computing accurately the epoch of minimum of an eclipsing variable," *Bulletin of the Astronomical Institutes of the Netherlands*, vol. 12, 1956.
- [11] D. R. Soderblom and J. R. King, "Solar-Type Stars: Basic Information on Their Classification and Characterization," Space Telescope Science Institute, [Online]. Available: <http://www2.lowell.edu/users/jch/workshop/drs/drs-p1.html>. [Accessed 17 August 2022].
- [12] H. Karttunen, P. Kroger, H. Oja, M. Poutanen and K. J. Donner, Eds., *Fundamental Astronomy*, Fourth Edition ed., Berlin: Springer-Verlag, 2003.
- [13] A. J. Burgasser, "SDSS J080531.84+481233.0: An Unresolved L Dwarf/T Dwarf Binary," *The Astronomical Journal*, vol. 134, pp. 1330-1336, 2007.
- [14] P. J. Castro, J. E. Gizis, H. C. Harris, G. N. Mace, J. D. Kirkpatrick, I. S. McLean, P. Pattarakijwanich and M. F. Skrutskie, "Discovery of Four High Proper Motion L Dwarfs, Including a 10 pc L Dwarf at the L/T Transition," *The Astrophysical Journal*, vol. 776, p. 126, 2013.
- [15] A. A. Henden and R. H. Kaitchuck, *Astronomical Photometry: A Text and Handbook for the Advanced Amateur and Professional Astronomer*, Richmond: Willmann-Bell, Inc., 1990.
- [16] D. S. Birney, G. Gonzalez and D. Oesper, *Observational Astronomy*, Second ed., Cambridge: Cambridge University Press, 2006.
- [17] "Percent Error and Percent Difference," NC State University Physics Department, [Online]. Available: https://www.webassign.net/question_assets/ncsucalcphysmech13/percent_error/manual.html. [Accessed 19 August 2022].
- [18] L. Tornqvist, P. Vartia and Y. O. Vartia, "How Should Relative Changes be Measured?," *The American Statistician*, vol. 39, no. 1, pp. 43-46, 1985.

APPENDIX

Extinction Theory and Application Process

We follow the derivation of atmospheric extinction corrections from [15] (their Appendix J.3), with slight modifications. The primary modification is defining the optical depth (τ_λ) differently. These modifications are made to have the extinction coefficient for spectroscopy be the same as that for photometry. Fig. 33 shows an illustration of flux ($F_{\lambda o}$) entering a medium with an absorption coefficient (α_λ), traveling a distance (ds), and leaving with a reduced amount of flux ($F_{\lambda o} - dF_\lambda$).

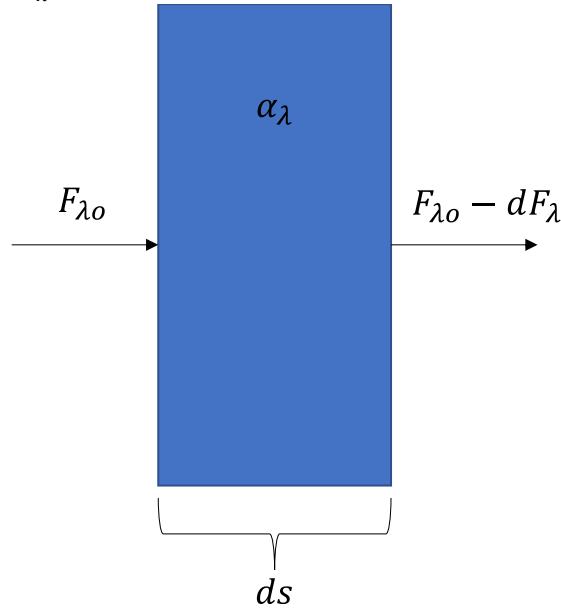


Fig. 33. Illustration of flux ($F_{\lambda o}$) entering a medium with an absorption coefficient (α_λ), traveling a distance (ds), and leaving with a reduced amount of flux ($F_{\lambda o} - dF_\lambda$).

$F_{\lambda o}$ is the flux at the top of the atmosphere, α_λ is the absorption coefficient indicating the fraction of flux lost per unit distance, dF_λ is the relative loss of light flux, and ds is the distance traveled for relative loss of light flux.

The relative loss of light flux can be expressed as Equation (11):

$$dF_\lambda = -F_\lambda \alpha_\lambda ds. \quad (11)$$

This can be rearranged as Equation (12):

$$\frac{dF_\lambda}{F_\lambda} = -\alpha_\lambda ds. \quad (12)$$

We can take the integral of both sides as shown in Equation (13):

$$\int_{F_{\lambda o}}^{F_\lambda} \frac{dF_\lambda}{F_\lambda} = \int_o^s -\alpha_\lambda ds. \quad (13)$$

Note that we are taking the flux from the top of the atmosphere ($F_{\lambda o}$) to the flux at the observer (F_λ) and the flux path from the position at the top of the atmosphere o to the observer with a total path length of s . This yields Equation (14) through Equation (16):

$$\ln(F_\lambda) \Big|_{F_{\lambda o}}^{F_\lambda} = - \int_o^s \alpha_\lambda ds \quad (14)$$

$$\ln(F_\lambda) - \ln(F_{\lambda o}) = - \int_o^s \alpha_\lambda ds \quad (15)$$

$$\ln\left(\frac{F_\lambda}{F_{\lambda o}}\right) = - \int_o^s \alpha_\lambda ds. \quad (16)$$

Taking the exponentiation of both sides, we get Equation (17) and Equation (18):

$$e^{\ln\left(\frac{F_\lambda}{F_{\lambda o}}\right)} = e^{-\int_o^s \alpha_\lambda ds} \quad (17)$$

$$\frac{F_\lambda}{F_{\lambda o}} = e^{-\int_o^s \alpha_\lambda ds}. \quad (18)$$

We arrive at an expression for the flux at the observer (F_λ) as a function of the flux at the top of the atmosphere ($F_{\lambda o}$) and the integral of the absorption coefficient of the atmosphere along the path it traveled, as shown in Equation (19):

$F_\lambda = F_{\lambda o} e^{-\int_o^s \alpha_\lambda ds}. \quad (19)$

A plane-parallel model of Earth's atmosphere is shown in Fig. 34. Light enters the atmosphere at an angle of z relative to the vertical and travels a distance s through the atmosphere. The vertical distance from the top of the atmosphere to the observer is given as y .

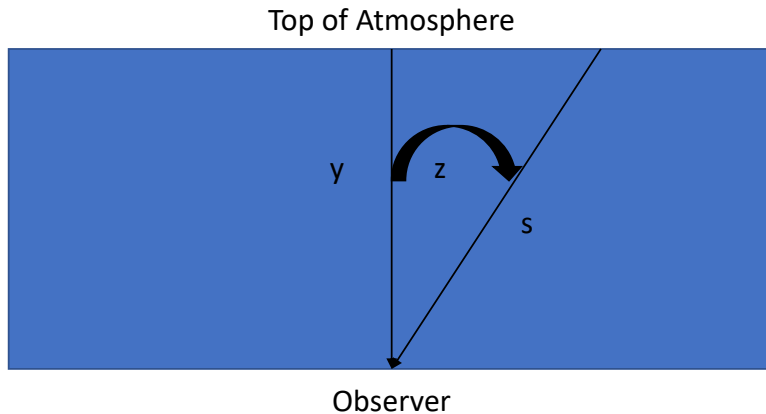


Fig. 34. Plane-parallel model of Earth's atmosphere.

The relationship between z , y , and s is shown in Equation (20):

$$\cos z = \frac{y}{s}. \quad (20)$$

The length of the path traveled by the flux is shown in Equation (21):

$$s = y \sec z. \quad (21)$$

Since the angle z is a constant, we can take the differential of both sides, yielding Equation (22):

$$ds = \sec z dy. \quad (22)$$

Substituting Equation (22) into Equation (19) we get Equation (23):

$$F_{\lambda} = F_{\lambda o} e^{-\int_0^y \alpha_{\lambda} \sec z dy} = F_{\lambda o} e^{-\sec z \int_0^y \alpha_{\lambda} dy}. \quad (23)$$

We can define the optical depth as Equation (24), the fractional flux loss:

$$\tau_{\lambda} = \int_0^y \alpha_{\lambda} dy. \quad (24)$$

Substituting Equation (24) into Equation (23) leads to Equation (25):

$$F_{\lambda} = F_{\lambda o} e^{-\tau_{\lambda} \sec z}. \quad (25)$$

If we let $\sec z = X$, where X the airmass, then Equation (25) becomes Equation (26):

$$F_{\lambda} = F_{\lambda o} e^{-\tau_{\lambda} X}. \quad (26)$$

Note that the airmass, X , given as $\sec z = X$, is an approximation for a plane-parallel model of the atmosphere and is accurate as long as the elevation is about ≥ 30 deg. For observations at an elevation lower than 30 deg, the airmass approximation quickly becomes inaccurate [16] (their page 127). The derivation here is valid for observations at an elevation of ≥ 30 deg.

Equation (26) can be rearranged to Equation (27) and Equation (28):

$$\frac{F_{\lambda}}{F_{\lambda o}} = e^{-\tau_{\lambda} X} \quad (27)$$

$$F_{\lambda o} = F_{\lambda} e^{\tau_{\lambda} X}. \quad (28)$$

If we take natural logarithm of both sides, we get Equation (29) through Equation (32):

$$\ln(F_{\lambda}) = \ln(F_{\lambda o} e^{-\tau_{\lambda} X}) \quad (29)$$

$$\ln(F_{\lambda}) = \ln(F_{\lambda o} e^{-\tau_{\lambda} X}) \quad (30)$$

$$\ln(F_{\lambda}) = \ln(F_{\lambda o}) + \ln(e^{-\tau_{\lambda} X}) \quad (31)$$

$$\ln(F_{\lambda}) = \ln(F_{\lambda o}) - \tau_{\lambda} X. \quad (32)$$

We arrive at Equation (33), an expression in terms of the flux at the observer (F_{λ}), the flux at the top of the atmosphere ($F_{\lambda o}$), the airmass (X), and the optical depth (τ_{λ}):

$$\ln(F_{\lambda}) = -\tau_{\lambda} X + \ln(F_{\lambda o}). \quad (33)$$

Relation to Photometry

We would like an expression that is in terms of the first-order extinction coefficient (k'_{λ}) used in photometry rather than the optical depth (τ_{λ}), which is the fractional flux loss. For photometry, we can start with the expression for the relation between magnitude difference and flux ratio, Equation (34) (Equation 1.3 from [15]):

$$m_1 - m_2 = -2.5 \log_{10} \left(\frac{F_1}{F_2} \right) \quad (34)$$

where m_1 is the magnitude of object 1, m_2 is the magnitude of object 2, F_1 is the flux of object 1, and F_2 is the flux of object 2. Now, we may apply this to the magnitude at the observer and top of the atmosphere for a single target, respectively, if we let subscript 1 be λ and subscript 2 be λ_o . Then we get Equation (35):

$$m_\lambda - m_{\lambda_o} = -2.5 \log_{10} \left(\frac{F_\lambda}{F_{\lambda_o}} \right). \quad (35)$$

Substituting Equation (27) into Equation (35), we get Equation (36):

$$m_\lambda - m_{\lambda_o} = -2.5 \log_{10}(e^{-\tau_\lambda X}) \quad (36)$$

which turns into Equation (37) and Equation (38):

$$m_\lambda - m_{\lambda_o} = 2.5 \log_{10}(e) \tau_\lambda X \quad (37)$$

$$m_{\lambda_o} = m_\lambda - 2.5 \log_{10}(e) \tau_\lambda X. \quad (38)$$

The expression of Equation (39) (Equation J.46 from [15]) is shown:

$$m_{\lambda_o} = m_\lambda - k'_\lambda X \quad (39)$$

where k'_λ is the first-order extinction coefficient from photometry. By comparison of Equation (38) and Equation (39), the first-order extinction coefficient of photometry has the relation of Equation (40):

$$k'_\lambda = 2.5 \log_{10}(e) \tau_\lambda. \quad (40)$$

Rearranging, we also have an expression for τ_λ in Equation (41):

$$\tau_\lambda = \frac{k'_\lambda}{2.5 \log_{10}(e)} \quad (41)$$

This expression relates the optical depth (τ_λ) defined here and the first-order extinction coefficient for photometry (k'_λ). Applying the extinction coefficient from photometry to our spectroscopy equation, we may solve for flux at the top of the atmosphere (F_{λ_o}). Substituting Equation (41) into Equation (28), we get the expression for flux at the top of the atmosphere in Equation (42):

$$F_{\lambda_o} = F_\lambda e^{\frac{k'_\lambda X}{2.5 \log_{10}(e)}} \quad (42)$$

The Extinction Coefficient (k_λ)

Substituting Equation (41) into Equation (33), we arrive at Equation (43):

$$\ln(F_\lambda) = \left(\frac{-k'_\lambda}{2.5 \log_{10}(e)} \right) X + \ln(F_{\lambda_o}). \quad (43)$$

This expression has the first-order extinction coefficient as defined for photometry. The extinction coefficient for broad-band photometry is composed of not just the first-order extinction coefficient (k'_λ) but also of higher orders of extinction coefficients, second-order extinction coefficient (k''_λ), etc. The second-order extinction coefficient (k''_λ) is dependent on the flux distribution of the observed target, or a color-dependent term. If the average extinction of a broad-band filter is used, since the extinction is larger for shorter wavelengths, a target whose flux peaks in the blue

would have its extinction underestimated, while a target whose flux peaks in the red would have its extinction overestimated, resulting in a systematic error. The second-order extinction coefficient takes into account the changing extinction across the broad-band filter.

Spectroscopy is composed of wavelength bins that are significantly smaller than the wavelength range of a broad-band filter (e.g., Johnson-Cousins B band). The Falcon Telescope Network has a spectral resolution of about 1.5 nm per pixels (1 nm per pixel for OJC). It is reasonable to assume that the second-order extinction (k'_λ) is negligible across the wavelength range of each spectral bin. Therefore, we express k'_λ as k_λ .

We now have the total extinction per unit wavelength for our spectroscopy as k_λ . We then get a final expression of Equation (44):

$$\ln(F_\lambda) = \frac{-k_\lambda}{2.5 \log_{10}(e)} X + \ln(F_{\lambda_0}). \quad (44)$$